

AD-A089 047

NAVAL RESEARCH LAB WASHINGTON DC

F/6 2 /8

STEADY STATE TREATMENT OF RELATIVISTIC ELECTRON BEAM EROSION.(U)

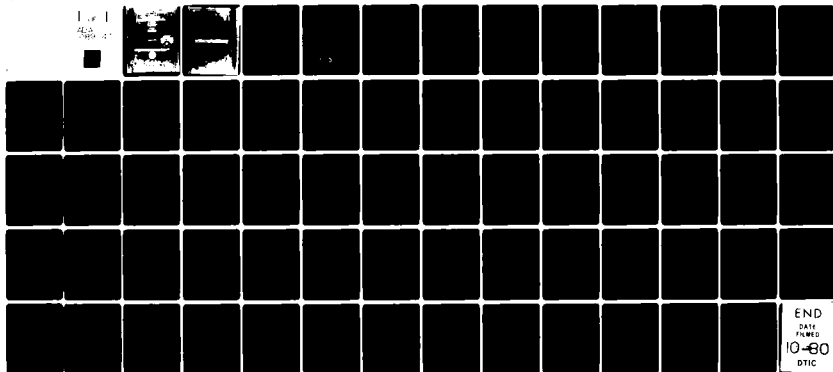
SEP 80 W M SHARP, M LAMPE

UNCLASSIFIED

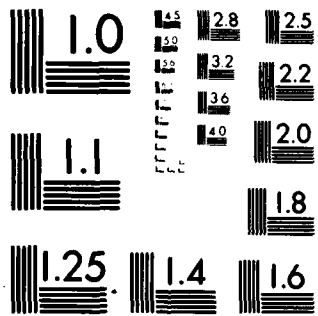
NRL-MR-4315

NL

1 of 1
444
100



END
DATE
FILMED
10-80
DTIC



MICROCOPY RESOLUTION TEST CHART
NATIONAL BUREAU OF STANDARDS-1963-A

AD A089042

SECURITY CLASSIFICATION OF THIS PAGE (When Data Entered)

CONTENTS

I.	INTRODUCTION.....	1
II.	MODEL.....	4
	A. Assumptions.....	4
	B. Envelope Equations.....	7
	C. Field Equations.....	10
	D. Conductivity Equations.....	17
	E. Boundary Conditions.....	20
	F. Solution of the Equations.....	23
III.	ANALYTIC AND NUMERICAL RESULTS.....	25
	A. Erosion Rate.....	26
	B. Dimensionless Equations.....	29
	C. Axial Profile of the Beam and Conducting Channel for $\kappa_0 = 0$	32
	1. General Considerations.....	32
	2. Validity of the Steady State Assumption.....	35
	3. Scaling of Beam Profile and Fractional Return Current with μ	36
	D. Axial Profiles and Scaling for $\kappa_0 \neq 0$	39
IV.	SUMMARY.....	42
	APPENDIX.....	44
	ACKNOWLEDGMENTS.....	46
	REFERENCES.....	47
	DISTRIBUTION LIST.....	59

DTIC
ELECTE
S **D**
 SEP 12 1980
B

ACCESSION for		
NTIS	White Section	<input checked="" type="checkbox"/>
DDC	Buff Section	<input type="checkbox"/>
UNANNOUNCED		<input type="checkbox"/>
JUSTIFICATION _____		
BY _____		
DISTRIBUTION/AVAILABILITY CODES		
Dist.	AVAIL.	and/or SPECIAL
A		

STEADY STATE TREATMENT OF RELATIVISTIC ELECTRON BEAM EROSION

I. INTRODUCTION

When a highly relativistic electron beam propagates through initially un-ionized gas, the radial forces due to space charge and the beam magnetic field nearly cancel at the beam head. Consequently the beam head is not self-pinched, and electrons there spread out radially at a rate governed by the beam emittance. Behind the freely expanding head, ionization of the background gas raises the conductivity and neutralizes the space charge, and the increasing beam azimuthal magnetic field pinches the beam to an equilibrium radius determined by the balance of beam pressure and the radial magnetic force. When the background gas is pre-ionized, current neutralization causes a similar expansion of the beam head, and beam pinching then occurs as the return current decays resistively. In either case the beam takes on a characteristic "trumpet" shape.

The continual expansion of the beam head causes the ionization rate near the head to drop. Consequently, the region where the pinch force builds up, referred to here as the "pinch point", moves back toward the body of the beam. This recession of the pinch point from the head slows down as the head radius becomes large, until a second effect becomes important: for a highly relativistic beam, energy loss due to the induced axial electric field ahead of the pinch point

reduces the relativistic mass of beam electrons and appreciably increases radial expansion. After an initial transient period of head expansion, the two effects together cause an almost steady movement of the pinch point back into the beam and a continual effective loss of the head. This beam head "erosion" can significantly affect the stability and propagation characteristics of a high-energy electron beam.

Several groups have studied beam head erosion and have informed us of their unpublished results. Both Biegalski¹ and Lee² have derived analytic estimates of the erosion rate using simple energy-balance arguments. To study beam structure and verify the predicted erosion rate scaling, Lee² and Brueckner³ have made time-dependent calculations of axial beam profiles using radially-averaged beam equations. Similar calculations have been carried out by Hubbard et al.⁴ and by Johnston et al.⁵ with more elaborate models of conductivity production and the beam fields.

The present work obtains erosion rates for relativistic electron beams by a different method. Since the erosion rate reaches an approximately constant value when the head has expanded sufficiently, we assume that the beam axial profile is stationary in a frame of reference moving with the pinch point. This assumption leads to a time-independent set of radially-averaged beam equations that we solve numerically to obtain both the pinch frame velocity and the axial beam profile. This method requires substantially less computation than time-dependent profile calculations and gives the erosion rate unambiguously. Details of the model are presented in Sec. II along with

the methods used to solve the beam equations. Section III gives results of the model: An analytic approximation of the beam head erosion rate is derived and used to reduce the beam equations to a simpler dimensionless form. These equations show that the beam axial profile depends principally on the dimensionless parameters that determine the gas conductivity. We propose analytic scaling laws for the beam radius, pinch force, and conductivity, and compare the analytic predictions with extensive numerical solutions. Section IV then summarizes the conclusions.

II. MODEL

A. Assumptions

The configuration considered here is an axisymmetric beam of relativistic electrons moving paraxially in the positive z direction. For convenience, the beam head position at time $t = 0$ is chosen to be $z = 0$, and the beam source is at $z = -\infty$. There are no externally-generated fields. We take the beam current I_b to be small compared with the Alfven limit $I_A = 17 (\gamma^2 - 1)^{1/2}$ kA, where γ is the relativistic factor of typical beam electrons. Since this requirement ensures that the transverse velocity of beam particles v_\perp is small compared with the axial velocity v_z , we make the "paraxial beam" approximation, consistently neglecting terms of the order of v_\perp^2/v_z^2 compared with unity. Also, we assume that $\gamma \geq 5$ everywhere, so that $v_z \approx c$, and the relative axial motion of beam electrons is negligible.

In this paper we do not consider instabilities, such as the well known resistive hose instability. The development of a beam is then a time-dependent axisymmetric process involving both the radial and axial dimensions. In this work we make three approximations that allow a one-dimensional time-independent formulation:

1. We take I_b , γ , and the beam emittance to be time-independent at the source throughout the pulse, and we neglect changes in beam emittance and energy due to collisions and radiation. These single-particle loss processes are instead assumed to cause only gradual paraxial changes in the beam erosion rate and axial profile. However, changes in γ due to the collective electromagnetic fields of the beam

are calculated self-consistently; these effects are very strong near the pinch point and are essential features of beam head evolution.

2. All beam quantities are assumed to depend on z and t only through the combination $\zeta \equiv V_p t - z$, where $V_p \equiv \beta c < v_z$ is the effective pinch-point velocity in the laboratory frame of reference. This assumption implies that the beam structure is stationary in a frame moving with velocity V_p . Although the beam head, located as ζ_0 , is obviously moving relative to this pinch frame when $V_p < v_z$, we show later that the expanded beam head near ζ_0 has little effect on the pinch structure when the radius at ζ_0 has become large compared with the pinched radius. Also, we assume that the beam tail, at $\zeta_L \equiv \zeta_0 + L$, is well behind the pinch point. Mathematically, the stationary-profile assumption implies that

$$\begin{aligned}\frac{\partial}{\partial t} &= \beta c \frac{\partial}{\partial \zeta} \\ \frac{\partial}{\partial z} &= - \frac{\partial}{\partial \zeta},\end{aligned}\tag{1}$$

where $\beta \equiv V_p/c$ must still be determined. Using the fact that $v_z \approx c \gg v_\perp$ for beam electrons, we also write all total time derivatives as

$$\frac{d}{dt} \approx \frac{\partial}{\partial t} + c \frac{\partial}{\partial z} = - (1 - \beta) c \frac{\partial}{\partial \zeta}.\tag{2}$$

3. The beam radial profile is assumed to change self-similarly as the beam radius expands. We therefore model the beam fields and current density and the background conductivity by functions of the form

$$f(r,\zeta) = f(0,\zeta) F(r/R), \quad (3)$$

where r is the radial coordinate, $R(\zeta)$ is the mean beam radius, and the radial envelopes $F(r/R)$ are functions with $F(0) = 1$. This assumption avoids a self-consistent calculation of the beam radial structure and permits analytic radial averaging of the beam equations. We find that calculated head erosion rates and axial profiles are insensitive to the choice of radial dependences.

With these assumptions, we can write the equations for the beam radius and energy and the radially-averaged fields and conductivity as a set of coupled ordinary differential equations in the variable ζ , with the dimensionless pinch-point velocity β appearing as a "nonlinear eigenvalue".

B. Envelope Equations

To clarify the assumptions involved, we review the derivation of the equations for the beam radius and mean particle energy from the single particle equation of motion. For a collisionless nonradiating electron in electric field \underline{E} and magnetic field \underline{B} , the relativistic equation of motion is

$$\frac{d}{dt} (\gamma \underline{v}) = - \frac{e}{m} \left(\underline{E} + \frac{\underline{v} \times \underline{B}}{c} \right), \quad (4)$$

where, $-e$ and m are respectively the electron charge and mass, and $\gamma \equiv (1 - \underline{v} \cdot \underline{v}/c^2)^{-1/2}$ is the ratio of total particle energy to rest energy mc^2 . The dot product of \underline{v} with (4) gives the energy equation

$$\frac{d\gamma}{dt} = - \frac{e}{mc^2} \underline{v} \cdot \underline{E}. \quad (5)$$

If terms of the order of $(v_{\perp}/c)^2$ and γ^{-2} are discarded, then (4) yields

$$\frac{d}{dt} \left(\gamma \frac{dr}{dt} \right) \approx - \omega_{\beta}^2 r, \quad (6)$$

where $\omega_{\beta}^2 \equiv -e(B_{\theta} - E_r)/(mr)$ is the nonrelativistic betatron frequency, and (5) reduces to

$$\frac{d\gamma}{dt} \approx - \frac{e}{mc} E_z. \quad (7)$$

Since beam electrons traverse much of the beam cross-section while performing betatron oscillations, it is a reasonable approximation to neglect any correlation between the energy $mc^2\gamma$ of an electron and its radial position r . (The limitations of this approximation, and effects due to spread γ and γ - r correlation, are discussed in Ref. 6.) We therefore assume γ is a function of t only and write an averaged form of (7),

$$\frac{dy}{dt} \approx -\frac{e}{mc} \mathcal{E}_z \equiv \frac{-e}{mc} \langle E_z \rangle \quad (8)$$

where \mathcal{E}_z is the average axial electric field acting on electrons in a thin beam segment. Explicitly, we define the average of any quantity $f(r, \zeta)$ over the beam cross section as

$$\langle f \rangle \equiv \frac{2\pi}{N_b} \int_0^\infty dr \, r \, n_b f, \quad (9)$$

where $n_b(r, \zeta)$ is the beam number density, and

$$N_b \equiv 2\pi \int_0^\infty dr \, r \, n_b \quad (10)$$

is the number of beam electrons per unit length.

To derive an equation for the root-mean-square beam radius R , appropriate moments of (6) are averaged over the beam cross section, and self-similar expansion is assumed (but it is not necessary to assume any particular self-similar form). The resulting envelope equation, derived in more general form by Lee and Cooper⁷, is

$$\frac{d}{dt} \left[\gamma R^3 \frac{d}{dt} \left(\gamma \frac{dR}{dt} \right) + \gamma R^2 \omega_\beta^2 r^2 \right] = 0. \quad (11)$$

The beam is assumed to be in quasi-static force balance at its tail, $\zeta = \zeta_L$, so that the time derivatives of γ and R vanish there. Slow variation of γ and R at the beam tail will be treated in Sec. IIE as a parametric variation of the boundary conditions. The first integral of (11) is then

$$\frac{d}{dt} \left(\gamma \frac{dR}{dt} \right) = \frac{e}{m} \left(\frac{U}{R} - \frac{\gamma_L R_L^2 U_L}{\gamma R^3} \right), \quad (12)$$

where $U \equiv \langle r(B_\theta - E_r) \rangle$, and the subscript L denotes quantities at ζ_L .

We use the steady-state relation (2) to rewrite (8) and (12) as time-independent equations for the beam radius and energy:

$$\frac{d}{d\zeta} \left(\gamma \frac{dR}{d\zeta} \right) = \frac{e}{(1-\beta)^2 mc^2} \left(\frac{U}{R} - \frac{\gamma_L R_L^2 U_L}{\gamma R^3} \right) \quad (13)$$

$$\frac{d\gamma}{d\zeta} = \frac{e}{(1-\beta) mc^2} \mathcal{E}_z. \quad (14)$$

C. Field Equations

Since the beam magnetic field only appears in (13) combined with the radial electric field in $U \equiv \langle r(B_\theta - E_r) \rangle$, we reduce Maxwell's equations to a pair of equations for $u \equiv r(B_\theta - E_r)$ and E_z . In the absence of external magnetic fields and azimuthal currents, the components of \underline{B} and \underline{E} in a cylindrical geometry are $\underline{B} = (0, B_\theta, 0)$ and $\underline{E} = (E_r, 0, E_z)$, and the pertinent components of Maxwell's equations in Gaussian units are

$$\frac{1}{r} \frac{\partial}{\partial r} (r B_\theta) = \frac{4\pi}{c} (J_z + \sigma E_z) + \frac{1}{c} \frac{\partial E_z}{\partial t}, \quad (15)$$

$$-\frac{\partial B_\theta}{\partial z} = \frac{4\pi}{c} (J_r + \sigma E_r) + \frac{1}{c} \frac{\partial E_r}{\partial t}, \quad (16)$$

$$\frac{\partial E_r}{\partial z} - \frac{\partial E_z}{\partial r} = -\frac{1}{c} \frac{\partial B_\theta}{\partial t}, \quad (17)$$

where J_r and J_z are components of the beam current density and σ is the scalar background conductivity. When (15) - (17) are written in terms of ζ using (1), the equations can be combined to give

$$(1 + \beta) \frac{\partial}{\partial \zeta} (B_\theta - E_r) + \frac{4\pi\sigma}{c} (B_\theta - E_r) = \frac{4\pi}{c} J_r + \frac{\partial E_z}{\partial r} + \frac{4\pi\sigma}{c} B_\theta \quad (18)$$

$$\frac{\partial E_z}{\partial r} = \frac{\partial}{\partial \zeta} (B_\theta - E_r) - (1 - \beta) \frac{\partial B_\theta}{\partial \zeta} \quad (19)$$

$$\frac{1}{r} \frac{\partial}{\partial r} (r B_\theta) = \beta \frac{\partial E_z}{\partial \zeta} + \frac{4\pi\sigma}{c} E_z + \frac{4\pi}{c} J_z. \quad (20)$$

The radial beam current J_r is eliminated by invoking charge conservation. In terms of ζ , the continuity equation is written

$$-e\beta c \frac{\partial n_b}{\partial \zeta} + \frac{1}{r} \frac{\partial}{\partial r} (r J_r) - \frac{\partial J_z}{\partial \zeta} = 0, \quad (21)$$

and with $J_z \approx -ecn_b$, this yields

$$J_r = \frac{1-\beta}{2\pi r} \frac{\partial I}{\partial \zeta} \quad (22)$$

where

$$I(r) \equiv 2\pi \int_0^r dr' r' J_z',$$

and J_z' denotes $J_z(r')$. Using (22), we rewrite (18) and (19) as a coupled pair of equations for u and E_z

$$(1+\beta) \frac{\partial u}{\partial \zeta} + \frac{4\pi\sigma}{c} u = \frac{2(1-\beta)}{c} \frac{\partial I}{\partial \zeta} + r \frac{\partial E_z}{\partial r} + \frac{4\pi\sigma}{c} r B_\theta, \quad (23)$$

$$E_z = \frac{\partial}{\partial \zeta} \int_{R_c}^r \frac{dr'}{r'} [u' - (1-\beta) r' B_\theta'], \quad (24)$$

with B_θ given explicitly by the integral of (20):

$$r B_\theta = \frac{2I}{c} + \frac{4\pi}{c} \int_0^r dr' r' \sigma' E_z' + \beta \frac{\partial}{\partial \zeta} \int_0^r dr' r' E_z'. \quad (25)$$

Here, E_z is taken to vanish at $r = R_c$. This cutoff radius for E_z is mathematically necessary to give the beam a finite inductance per unit length, and it corresponds physically to the radius at which the conductivity becomes too small to cause charge neutralization. Normally R_c is determined by the extent of induced breakdown around the beam

head and is large compared with the fully pinched radius R_L . Since the cutoff radius enters the field equations only logarithmically, we take R_c to be constant. When $1-\beta \ll 1$, (23), (24), and (25) reduce approximately to the single equation

$$\frac{\partial u}{\partial \zeta} + \frac{4\pi\sigma}{c} u \approx \left[\frac{2I}{c} + \frac{\partial}{\partial \zeta} \int_0^r dr' r' \kappa \int_{R_c}^r dr'' \frac{u''}{r''} + \frac{\partial^2}{\partial \zeta^2} \int_0^r dr' r' \int_{R_c}^r dr'' \frac{u''}{r''} \right], \quad (26)$$

with the supplementary relation

$$E_z \approx \frac{\partial}{\partial \zeta} \int_{R_c}^r dr' \frac{u'}{r'} \quad (27)$$

For typical high- γ beams, we find that $1-\beta \leq 0.2$, justifying the use of (26) and (27). We note that $1-\beta$ is retained in (13) and (14), where it is obviously important.

To obtain equations for $U \equiv \langle u \rangle$ and \mathcal{E}_z , we choose specific self-similar expressions for n_b , u , and σ with the form of (3), and average the field equations (26) and (27) according to (9). Since the number density of a relativistic beam in an initially uniform neutral gas changes from an approximately Gaussian radial envelope

$$n_b(r, \zeta) = \frac{N_b}{\pi R^2(\zeta)} \exp(-r^2/R^2) \quad (28)$$

in the freely expanding head to a Bennett profile⁸

$$n_b(r, \zeta) = \frac{N_b}{\pi R^2(\zeta)} \frac{1}{(1 + r^2/R^2)^2} \quad (29)$$

in the pinched region, either of these forms might be used for n_b . In most numerical calculations, we use the Gaussian profile (28). For

comparison, calculations are also carried out using a cutoff Bennett distribution,

$$\begin{aligned} n_b(r, \zeta) &= 1.255 \frac{N_b}{\pi R^2(\zeta)} \frac{1}{(1 + r^2/R^2)^2}, & r \leq 1.98R, \\ n_b(r, \zeta) &= 0, & r > 1.98R, \end{aligned} \quad (30)$$

and a square distribution,

$$\begin{aligned} n_b(r, \zeta) &= \frac{N_b}{2\pi R^2(\zeta)}, & r \leq 2^{1/2}R, \\ n_b(r, \zeta) &= 0, & r > 2^{1/2}R, \end{aligned} \quad (31)$$

where the cutoff radii have been chosen so that $\langle r^2 \rangle = R^2$. We show later that the calculated erosion rates and axial profile are not sensitive to the form chosen for n_b .

The pinch force u is assumed to have the same radial dependence as rB_θ for the beam current alone. This choice is equivalent to assuming that fractional neutralization of the beam current and space charge is uniform over the beam cross section. For a Gaussian beam density profile, u is then given by

$$u = 2U[1 - \exp(-r^2/R^2)], \quad (32)$$

and analogous analytic expressions are readily found for the Bennett and square beam profiles.

For a beam propagating into an initially un-ionized or weakly ionized gas, the gas conductivity is due primarily to direct ionization by the beam. The radial conductivity profile is therefore expected to be qualitatively similar to the beam density profile. However, the

conductivity profile at any ζ is typically broader than the beam density profile at the same position, because the gas ionization is due to the more expanded part of the beam ahead of ζ . In addition, such effects as electric breakdown and beam-generated radiation can result in broad, weakly-conducting radial wings. As with the beam density profile, we do not attempt a self-consistent calculation of the radial conductivity structure. Instead, we specify an analytic self-similar form for the radial dependence of σ and examine the sensitivity of calculated results to this choice. For the Gaussian density profile (29), we assume the form

$$\sigma(r, \zeta) = \sigma(0, \zeta) \exp [-\alpha r^2 / R^2(\zeta)], \quad (33a)$$

where α is a constant between zero and unity which can be used to vary the breadth of the conductivity profile relative to the beam profile. We find that the results of numerical calculations are quite insensitive to the choice of α , which justifies the use of simple self-similar models. For beams with the cut-off Bennett density profile (30), we use the unbroadened conductivity profile

$$\sigma(r, \zeta) = \frac{\sigma(0, \zeta)}{[1 + r^2 / R^2(\zeta)]^2}, \text{ for } r \leq 1.98R, \quad (33b)$$

and for the square density profiles (31) we take

$$\sigma(r, \zeta) = \sigma(0, \zeta), \quad \text{for } r \leq 2^{1/2}R \quad (33c)$$

The calculation of $\sigma(0, \zeta)$ is discussed in the next section.

The radially-averaged quantity $\kappa \equiv 4\pi\langle\sigma\rangle/c$ occurs frequently in the averaged field equations. For each of the three beam profiles,

$\kappa(\zeta)$ is related to $\sigma(0, \zeta)$ by

$$\kappa(\zeta) = (1+\alpha)^{-1} 4\pi\sigma(0, \zeta)/c, \quad \text{Gaussian,} \quad (34a)$$

$$\kappa(\zeta) = (0.415) 4\pi\sigma(0, \zeta)/c, \quad \text{cut-off Bennett,} \quad (34b)$$

$$\kappa(\zeta) = 4\pi\sigma(0, \zeta)/c, \quad \text{square.} \quad (34c)$$

With these assumed radial dependences, a straightforward but lengthy calculation gives the radial averages of (26) and (27). For each of the three radial density profiles the equations take the form

$$A \frac{d^2 U}{d\zeta^2} + B \frac{dU}{d\zeta} - CU = \kappa \left(\frac{I_b}{c} - U \right), \quad (35)$$

$$\mathcal{E}_z = - \frac{d}{d\zeta} (\lambda U) - \frac{U}{R} \frac{dR}{d\zeta} + D \frac{dU}{d\zeta}, \quad (36)$$

where $\lambda \equiv \ln(R_c^2/R^2)$. For a Gaussian density profile with the conductivity profile (34), the coefficients in (35) are

$$A = \frac{2+\alpha}{4(1+\alpha)} \left[\lambda + \ln\left(\frac{1+\alpha}{2+\alpha}\right) + \gamma_E \right] \kappa R^2, \quad (37a)$$

$$B = \frac{2+\alpha}{2} \left\{ 1 + \frac{1+\alpha}{2(1+2\alpha)} \left[\lambda + \ln\left(\frac{1+2\alpha}{2(1+\alpha)}\right) + \gamma_E \right] \kappa^2 R^2 \right\} - \kappa R \frac{dR}{d\zeta}, \quad (37b)$$

$$C = \frac{2+\alpha}{2} \left(1 + \frac{1}{2} \kappa^2 R^2 \right) \frac{1}{R} \frac{dR}{d\zeta} + \frac{1}{2} \kappa R^2 \left[\frac{1}{R} \frac{d^2 R}{d\zeta^2} - \frac{\alpha}{2+\alpha} \left(\frac{1}{R} \frac{dR}{d\zeta} \right)^2 \right], \quad (37c)$$

$$D = \ln 2 + \gamma_E, \quad (37d)$$

where $\gamma_E = 0.5772$ is Euler's constant. For the cut-off Bennett density profile with a Bennett conductivity profile of the same width, we find

$$A = (0.36\lambda + 0.51) \kappa R^2, \quad (38a)$$

$$B = 1.59 + (0.46\lambda + 0.15)\kappa^2 R^2 - 0.91\kappa R \frac{dR}{d\zeta}, \quad (38b)$$

$$C = (1.50 + 0.70\kappa^2 R^2) \frac{1}{R} \frac{dR}{d\zeta} + \left[0.45 \frac{1}{R} \frac{d^2 R}{d\zeta^2} - 0.34 \left(\frac{1}{R} \frac{dR}{d\zeta} \right)^2 \right] \kappa R^2 \quad (38c)$$

$$D = 0.111. \quad (38d)$$

When the density and conductivity have square radial profiles extending to $2^{1/2}R$, the coefficients are

$$A = \frac{1}{2} \left(\lambda + \frac{2}{3} - \ln 2 \right) \kappa R^2, \quad (39a)$$

$$B = 1 + \frac{1}{2} \left(\lambda + \frac{2}{3} - \ln 2 \right) \kappa^2 R^2 - \frac{4}{3} \kappa R \frac{dR}{d\zeta}, \quad (39b)$$

$$C = \left(2 + \frac{2}{3} \kappa^2 R^2 \right) \frac{1}{R} \frac{dR}{d\zeta} + \frac{2}{3} \kappa R \frac{d^2 R}{d\zeta^2}, \quad (39c)$$

$$D = \ln 2 - \frac{1}{2}. \quad (39d)$$

D. Conductivity Equations

The processes governing the evolution of the gas conductivity can be modeled at various levels of completeness and accuracy. In this work, we use the simplest model which is appropriate for weakly-ionized gases, the regime of principal interest to us. In this regime, the conductivity is related to the background electron number density n_e by

$$\sigma = \frac{n_e e^2}{m \nu_m} . \quad (40)$$

Here, ν_m is the electron-molecule momentum transfer collision frequency, which is proportional to the gas density and only weakly dependent on electron temperature T_e . For dry air,

$$\nu_m \approx 1.4 \times 10^{12} T_e^{1/2} \bar{\rho} \text{ sec}^{-1} , \quad (41)$$

where T_e , in units of eV, is between 0.5 and 10, and $\bar{\rho}$ is the air density normalized to the density of air at standard temperature and pressure.

We model the electron density as

$$\frac{\partial n_e}{\partial t} = \hat{A}_1 \bar{\rho} |J_b| - \hat{A}_2 (T_e) \bar{\rho} n_e^2 + \hat{A}_3 (T_e) \bar{\rho} n_e , \quad (42)$$

where the first term represents direct ionization by beam electron impact, the second term represents three-body recombination and the third term represents ionization by secondary electron impact, the process which leads to electric breakdown. Since \hat{A}_1 is independent of T_e and the temperature dependence of \hat{A}_2 is fairly weak, we take both

coefficients to be constant. In contrast, \hat{A}_3 increases sharply with T_e , particularly for $T_e \geq 5\text{eV}$. To model breakdown accurately, we would either have to include an equation for T_e in the formalism or use some phenomenological relation giving \hat{A}_3 in terms of quantities that determine T_e , such as the ratio of electric field to gas density. We note, however, that for $\bar{\rho} \geq 0.1$, secondary ionization is usually only a small correction to primary beam ionization, except in the radial wings outside the beam. The reason is that T_e is large only in front of the pinch point where substantial E_r and E_z fields occur, but n_e is small enough here that primary ionization dominates secondary production. We therefore ignore the \hat{A}_3 term and use temperature-independent approximate values of \hat{A}_2 and v_m . We then use (40) and (34) to rewrite (42) with $r = 0$ as an equation for the radially averaged quantity κ

$$\beta \frac{d\kappa}{d\zeta} = \frac{A_1 |I_b|}{R^2} - A_2 \bar{\rho}^2 \kappa^2, \quad (43)$$

where

$$A_1 = \eta_1 \frac{4e^2 \hat{A}_1}{mc^2 v_m / \bar{\rho}}, \quad (44)$$

$$A_2 = \eta_2 \frac{m(v_m / \bar{\rho}) \hat{A}_2}{4\pi e^2}, \quad (45)$$

and η_1 and η_2 are geometric factors, given by

$$\eta_1 = \begin{cases} (1 + \alpha)^{-1}, & \text{Gaussian} \\ 0.520 & , \text{ cut-off Bennett} \\ 0.5 & , \text{ square} \end{cases} \quad (46)$$

$$\eta_2 = \begin{cases} 1 + \alpha & , \text{ Gaussian} \\ 2.41 & , \text{ cut-off Bennett} \\ 1 & , \text{ square} \end{cases} \quad (47)$$

Values of \hat{A}_1 , A_1 , and $v_m/\bar{\rho}$ are shown in Table 1 for several gases at $T_e = 2\text{eV}$. The recombination rate has little effect on either beam head erosion or beam structure near the head, the principal subjects treated here. In all calculations presented in Sec. III we use a typical value for air $A_2 = 8.7 \times 10^{-6}$. We note that as $\zeta \rightarrow \infty$, κ approaches an asymptotic value given by

$$\kappa_\infty R_\infty = \left(\frac{A_1 |I_b|}{A_2 \bar{\rho}} \right)^{1/2} \quad (48)$$

Our interest is principally in the regime where $\kappa_\infty R_\infty \gg 1$. For large ζ the beam space charge is then neutralized, the beam pinch force is magnetostatic, and the magnetic decay length is long compared to the beam radius. For air at standard density, $\kappa_\infty R_\infty > 100$ if $|I_b| \geq 0.3\text{kA}$, and the assumption that the air be weakly ($\leq 1\%$) ionized is satisfied if $|I_b|/R^2 \leq 5 \times 10^3 \text{ kA cm}^{-2}$.

E. Boundary Conditions

The envelope equation (13), energy equation (14), field equations (35) - (39), and conductivity equation (43) form a complete set of equations for R , γ , U , \mathcal{E}_z , and κ . Since the R and U equations are second order and the \mathcal{E}_z equation is zero order, six boundary conditions are required. For a highly relativistic beam, the fields ahead of ζ_0 vanish, so appropriate boundary conditions for κ and U are

$$U(\zeta_0) \equiv U_0 = 0 \quad (49)$$

$$\kappa(\zeta_0) \equiv \kappa_0 \geq 0, \quad (50)$$

where the subscript zero hereafter labels quantities at $\zeta = \zeta_0$. The initial conductivity κ_0 may be chosen to model any degree of pre-ionization.

To obtain boundary conditions at the beam tail ζ_L , we assume that the tail is far enough behind the pinch point that the beam is in quasi-static force balance at ζ_L . The appropriate boundary conditions are then

$$\gamma(\zeta_L) = \gamma_L, \quad (51)$$

$$R(\zeta_L) = R_L, \quad (52)$$

$$\left. \frac{dR}{d\zeta} \right|_{\zeta_L} = \epsilon^2 \frac{d}{d\zeta} \frac{1}{(\gamma U)^{1/2}} \Big|_{\zeta_L}, \quad (53)$$

$$U(\zeta_L) \equiv U_L = \frac{\epsilon}{\gamma_L R_L^2}, \quad (54)$$

where $\epsilon = \gamma_L U_L R_L^2$ is the beam emittance at ζ_L . To relate ϵ to the

beam source characteristics, we assume that electrons at ζ_L have not undergone significant ohmic energy loss. This assumption is usually a good approximation because ohmic dissipation is found to be concentrated ahead of the pinch point. If single particle energy loss mechanisms and beam-gas scattering are then neglected, γ_L and ϵ are equated with the values at the beam source. If energy loss by ionizing collisions and bremsstrahlung are included, the slow variation of γ with the distance of the beam tail from the source is given by⁹

$$\frac{d\gamma}{dz} = -\frac{\gamma}{\lambda_r} - 4\pi n_o Z \left(\frac{e^2}{mc^2} \right)^2 \ln \left(\frac{\pi mc^2 \gamma^{3/2}}{ZW_r} \right) \quad (55)$$

and the slow variation of ϵ , due to scattering, is given by^{7,10}

$$\frac{d\epsilon^2}{dz} = \frac{4\pi R^2 c^2}{\lambda_r} \frac{\hbar c}{e^2}, \quad (56)$$

where λ_r is the electron bremsstrahlung radiation length, given by⁹

$$\lambda_r^{-1} = 4 n_o Z(Z+1) \frac{e^2}{\hbar c} \left(\frac{e^2}{mc^2} \right)^2 \ln (183Z^{-1/3}), \quad (57)$$

$W_r \approx 13\text{eV}$, and n_o and Z are respectively the number density and effective nuclear charge of the background gas. In air at standard density $\lambda_r \approx 270$ meters, and the second term in (55) is of the order of 200-300 keV/m.

By adjusting the boundary values at ζ_L in this way, we can account for the slow variation of γ_L and ϵ with z due to single particle processes, while including the fast variations due to collective fields directly in the beam equations.

It is frequently convenient to consider a "semi-infinite" beam, i.e. one which is long enough so that the plasma return current

has effectively decayed away at the tail. In this case

$$U_L = U_\infty = I_b/c, \quad (58)$$

and the boundary conditions (53a) and (54a) become simply

$$R_L^2 \rightarrow R_\infty^2 = \frac{\epsilon^2 c}{\gamma_L^2 I_b}, \quad (52)$$

$$\left. \frac{dR}{d\zeta} \right|_{\zeta_L} \rightarrow \left. \frac{dR}{d\zeta} \right|_{\infty} = 0. \quad (53)$$

A highly relativistic beam of finite length can always be regarded as equivalent to the front end of a "semi-infinite" beam with properly chosen values, γ_∞ and R_∞ , at $\zeta = \infty$, since information propagates only backward in the beam. Thus the idea of a semi-infinite beam is quite general, and it is convenient to use R_∞ , γ_∞ and U_∞ as scaling factors for dimensionless coordinates.

Although the boundary conditions (49) - (54) are sufficient to determine the five quantities R , γ , U , \mathcal{E}_z , and κ as functions of ζ , one further constraint is needed to determine the pinch point velocity βc . This additional condition follows from the requirement that a steady state exist. After the transient initial beam head expansion, the beam axial profile should approach an isomorphous limit as the radius at the head R_0 continues to increase, and β should approach some limiting value. In our time-independent formulation, we must therefore find solutions with

$$\frac{R_0}{R_\infty} \gg 1,$$

and require that β be insensitive to the exact value of R_0 in this limit.

F. Solution of the Equations

The nonlinearity of the beam equations and the mixed boundary conditions preclude solution either by standard finite-difference methods or by numerical integration. Instead, we use the iterative method summarized in Fig. 1, which is convenient for the "semi-infinite" beam model discussed in Sec. IIE. We define $\hat{\zeta} \equiv \zeta - \zeta_0$, and choose a test value of β , which we denote by $\tilde{\beta}$. We then calculate the beam axial profile over an interval $0 < \hat{\zeta} < L$ that is chosen large enough that all quantities effectively reach their $\hat{\zeta} = \infty$ values. To start the iteration, we take U to have the form

$$U^{(0)} = U_{\infty} [1 - \exp(-\xi \frac{\hat{\zeta}}{L}) + \frac{\hat{\zeta}}{L} \exp(-\hat{\xi})], \quad (59)$$

where we use parenthesized superscripts to identify the successive iterates. This expression satisfies the boundary conditions $U_0 = 0$ and $U_L = U_{\infty}$, and the coefficient ξ can be chosen to give a suitable scale length. We calculate $R^{(0)}$ and $\gamma^{(0)}$ by numerically integrating the envelope equations (13) and (14) from $\hat{\zeta} = L$, and $R^{(0)}$ is then used in integrating the conductivity equation (43) from $\hat{\zeta} = 0$. Since the U equation (35) is a linear ordinary differential equation with known boundary values, it is readily reduced to tridiagonal matrix form and solved numerically for the first iterate $U^{(1)}$. This sequence of calculations is repeated until no significant change in the beam axial profile occurs with successive iterations. Since the only undetermined boundary value is the beam head radius R_0 , a convenient criterion for iteration convergence is that the quantity $|R_0^{(n+1)} - R_0^{(n)}|/R_0^{(n)}$

be less than some prescribed error limit for one or more successive iterations. This procedure is found to converge reliably for $\kappa_{\infty} R_{\infty} \geq 1$ and $R_0/R_{\infty} \leq 50$, provided that the finite-difference grid in the U calculation is fine enough to resolve the beam head structure.

To determine the pinch point velocity, we systematically vary $\tilde{\beta}$ to find solutions of the beam equations with $R_0/R_{\infty} \gg 1$. Figure 2 shows a typical plot of R_0 vs $\tilde{\beta}$. The increase of R_0 with $\tilde{\beta}$ occurs because the velocity of beam electrons relative to the pinch point, $v_z - v_p \approx (1-\tilde{\beta})c$, is reduced as $\tilde{\beta}$ increases. Consequently, beam electrons traversing the pinch region are subjected to the induced E_z there for a longer time, and the resulting reduction in γ drives radial expansion. The upper limit of $\tilde{\beta}$ is reached when the energy loss approximately equals the initial kinetic energy $(\gamma_{\infty}-1)mc^2$. This $\tilde{\beta}$ value maximizes R_0/R_{∞} , and the corresponding value of $\tilde{\beta}c$ should equal the physical pinch point velocity $v_p = \beta c$, provided that the assumptions $1-\beta \ll 1$ and $R_c^2/R_0^2 \ll 1$ are also satisfied. Because R_0 increases sharply as $\tilde{\beta} \rightarrow \beta$, the limiting value is easily estimated and, as required, is insensitive to the calculated beam head radius. The erosion rate, defined as the speed at which the pinch point recedes from the beam head, is then $v_z - v_p \approx (1-\beta)c$.

III. Analytic and Numerical Results

The basic equations (13) for R , (14) for γ , (35) - (39) for U and \mathcal{E}_z , and (43) - (47) for κ are quite complicated, and the dependence of the erosion rate and other quantities on the beam parameters is not immediately evident from these equations. However, a simple formula for the erosion rate can be derived when corrections of order $\lambda^{-1} \equiv [\ln(R_C^2/R^2)]^{-1}$ are neglected. Using this formula and again neglecting terms of order λ^{-1} , the equations for R , γ , U , \mathcal{E}_z and κ can be written in a much more concise dimensionless form that displays the parametric dependences. These simplified equations, together with data obtained from numerical solutions of the equations, show that the essential features of the axial profiles $R(\zeta)$, $\gamma(\zeta)$, $U(\zeta)$ and $\kappa(\zeta)$ can be described in terms of scaling with the dimensionless parameters which control the background conductivity. This program will be carried out in the remainder of this section. The approximate analytic results and scaling relations will be compared to extensive exact numerical solutions of (13), (14), (35)-(39), and (43)-(47) obtained by methods described in Sec. II.

A. Erosion Rate

When a steady state exists, a scaling law for the erosion rate follows almost immediately from the equations that determine energy flow along the beam. Approximate scaling laws have previously been obtained^{1,2} by a similar argument, in which the ohmic energy loss of the beam is equated with some estimated fraction of the kinetic energy lost through erosion.

The electron energy as a function of ζ is given by the integral of (14),

$$\gamma(\zeta) - \gamma_0 = \frac{e}{(1-\beta)mc^2} \int_{\zeta_0}^{\zeta} d\zeta' \mathcal{E}_z(\zeta') \quad (60)$$

Here, the time variation of γ is due to ohmic loss and the steady state assumption has been used to express it as a ζ variation. From (36),

\mathcal{E}_z is given by

$$\mathcal{E}_z \approx - \frac{d}{d\zeta} (\lambda U), \quad (61)$$

where the last two terms of (36) are neglected, since they are smaller than the first by a factor of order $\lambda^{-1} \ll 1$. Substituting (61) into (60) and using $U_0 = 0$ then gives the dimensionless erosion rate

$$1 - \beta = \frac{e}{mc^3} \frac{\lambda(\zeta) |U(\zeta)|}{\gamma(\zeta) - \gamma_0} \quad (62)$$

for any ζ . If ζ is well behind the pinch point, then $\lambda(\zeta) \approx \lambda_\infty$ and $U(\zeta) \approx I_n(\zeta)/c$, where the net current I_n is the beam current less the plasma return current. Moreover, $\gamma(\zeta) \gg \gamma_0$ for all cases with

$\gamma(\zeta) \gg 1$, as discussed in Sec. IIF and shown in what follows. In such cases, (62) reduces to

$$1 - \beta \approx \frac{e}{mc^3} \frac{\lambda_\infty |I_n(\zeta)|}{\gamma(\zeta)}, \quad (63)$$

which shows that $|I_n|/\gamma$ is approximately constant behind the pinch point. For a semi-infinite beam, defined as one that is long compared with the magnetic decay length, we can evaluate (63) at $\zeta = \infty$, where $I_n = I_b$ and γ is also known. We then obtain an explicit formula for the erosion rate,

$$1 - \beta = \frac{e}{mc^3} \frac{\lambda_\infty |I_b|}{\gamma_\infty} \equiv \frac{\lambda_\infty |I_b|}{I_A}. \quad (64)$$

The last expression relates the erosion rate to the familiar ratio of I_b to the Alfvén current I_A .

The argument leading to (64) is valid only when $1 - \beta$ is small because the \mathcal{E}_2 relation (61) was derived by assuming that $\beta \approx 1$. A more general derivation given in Appendix A shows that

$$1 - \beta \approx \left(1 + \frac{mc^3}{e} \frac{\gamma_\infty - 1}{\lambda_\infty |I_b|} \right)^{-1}, \quad (65)$$

which is valid for any β , and reduces to (64) when $1 - \beta \ll 1$.

Numerical solutions of (13), (14), (35) - (39), and (43)-(47), in which the beam current and ionization coefficient A_1 are varied over two orders of magnitude, substantiate the accuracy of (64). The erosion rate is quite independent of the coefficients that govern conductivity $\kappa(\zeta)$, even though these coefficients strongly affect the ζ dependence of R , κ , U , and γ . The erosion rate is also insensitive to the choice of beam profile (Gaussian, Bennett or square) and to the

parameter α in (33a), which strongly varies the width of the conducting channel. Table 2 compares calculated erosion rates with values given by Eq. (64) for a very broad range of γ , with $\kappa_0 = 0$ (initially neutral gas) and conductivity coefficients given by Table 1 for air. Other beam parameters are chosen to typify the new generation of linear induction accelerators being developed at Lawrence Livermore Laboratory. The calculated values of $1 - \beta$ are consistently about 13% below the estimates. This inaccuracy is within the error expected from the estimate (61) of \mathcal{E}_z . The scaling of $1 - \beta$ with I_b , γ_∞ and λ is accurately predicted by (64).

The erosion rate expression indicates that the existence of a steady non-zero erosion rate depends on ohmic energy loss: if $\gamma(\zeta) - \gamma_0$ vanishes, then (62) gives the physically meaningless result $1 - \beta = \infty$. We have verified this dependence by redoing the numerical solutions with γ held constant, rather than being determined by (14). The steady state model fails to produce a meaningful solution in this case. We believe that expansion and erosion of the beam head will occur even if γ is held constant, but not as a steady-state process.

B. Dimensionless Equations

Numerical solutions of the beam equations (13), (14), (35)-(39), and (43)-(47) over a wide range of parameters indicate several approximations that can be made with little loss of accuracy in the calculated quantities $R(\zeta)$, $\kappa(\zeta)$, $U(\zeta)$, $\gamma(\zeta)$, and the erosion rate $1-\beta$:

- (i) The choice of radial beam density profile $n_b(r)$ has little effect on the results. When profiles are calculated using Gaussian, Bennett, and square density profiles, the corresponding quantities typically differ by less than 3%.
- (ii) Varying the parameter α in (33a), which controls the shape of the radial conductivity profile, has a comparably small effect on results, even though $\alpha = 1$ corresponds to a conducting channel of the same radius as the beam, while $\alpha = 0$ corresponds to a constant conductivity out to a radius R_c which is orders of magnitude larger.
- (iii) The terms in the field equation (35) which arise from displacement current terms in (15) and (16) also affect the results by only a few percent, provided that $A_1 |I_b| \geq 0.1$. Neglecting these terms eliminates the second derivative in (35) and greatly simplifies the equation. We could not have predicted the validity of this approximation from the equations. Due to the very rapid variation with ζ in the beam head, the displacement current terms are not obviously negligible.
- (iv) Calculated axial profiles are insensitive to parameter changes that alter the erosion rate but leave the conductivity

generation rate unchanged. When γ_∞ is varied between 50 and 1000 while other parameters are held constant, $R(\zeta)$, $U(\zeta)$ and $\kappa(\zeta)$ are effectively unchanged, even though $1-\beta$ changes by more than an order of magnitude.

We now use these results to write the beam equations in a much simplified dimensionless form. For specificity, we consider a Gaussian beam profile and a flat conductivity profile ($\alpha = 0$). According to (i) and (ii), the results are not sensitive to these choices. In (35) and (37) we neglect the displacement current terms discussed in (iii), as well as terms that are corrections of order λ^{-1} . We explicitly use (64) for $1-\beta$ in Eqs. (13) and (14). Finally, we choose a suitable set of dimensionless variables,

$$\bar{U} \equiv U/U_\infty \equiv cU/I_b, \quad (66a)$$

$$\bar{R} \equiv R/R_\infty, \quad (66b)$$

$$\bar{\gamma} \equiv \gamma/\gamma_\infty, \quad (66c)$$

$$\bar{\kappa} \equiv \kappa R_\infty, \quad (66d)$$

$$\bar{\zeta} \equiv \zeta/R_\infty. \quad (66e)$$

Equations (13), (14), (35)-(37), and (43) can then be recast as

$$\frac{d\bar{U}}{d\bar{\zeta}} = \frac{1}{1 + \frac{1}{8} \lambda \bar{\kappa}^2 \bar{R}^2} \left[\bar{\kappa} (1-\bar{U}) + \left(1 + \frac{1}{8} \bar{\kappa}^2 \bar{R}^2\right) \frac{\bar{U}}{\bar{R}} \frac{d\bar{R}}{d\bar{\zeta}} \right], \quad (67)$$

$$\frac{d}{d\bar{\zeta}} \bar{\gamma} \frac{d\bar{R}}{d\bar{\zeta}} = - \frac{1}{\lambda_\infty (1-\beta)} \left(\frac{\bar{U}}{\bar{R}} - \frac{1}{\bar{\gamma} \bar{R}^3} \right), \quad (68)$$

$$\frac{d\bar{\gamma}}{d\bar{\zeta}} = -\frac{1}{\lambda_{\infty}} \frac{d}{d\bar{\zeta}} (\lambda \bar{U}) , \quad (69)$$

$$\frac{d\bar{\kappa}}{d\bar{\zeta}} = \frac{\mu}{\bar{R}^2} - A_2 \bar{\rho}^2 \bar{\kappa}^2 , \quad (70)$$

where

$$\mu \equiv A_1 |I_b| . \quad (71)$$

In this dimensionless form, the quantities $\bar{U}(\bar{\zeta})$, $\bar{\gamma}(\bar{\zeta})$, $\bar{R}(\bar{\zeta})$, and $\bar{\kappa}(\bar{\zeta})$ depend only the dimensionless parameters μ , A_2 , $1-\beta$, and the dimensionless pre-existing gas conductivity $\bar{\kappa}_0 \equiv \kappa_0 R_{\infty}$, if κ_0 is nonzero. However, the results are insensitive to $1-\beta$, as discussed in (iv). This results from the structure of (68): Since $\bar{R} \gg 1$ and $\bar{U} \approx 0$ near the beam head, (68) reduces there to $\gamma dR/d\bar{\zeta} \approx \text{constant}$. In the pinched region $\gamma dR/d\bar{\zeta}$ is small and slowly varying, so that the envelope equation gives the quasi-equilibrium condition $\bar{R} \approx (\bar{\gamma}\bar{U})^{1/2}$. For any $\bar{U}(\bar{\zeta})$, therefore, the erosion rate enters (68) only in the smooth transition between these limits. Also, since we are interested principally in the beam structure around the pinch point, where recombination is typically unimportant, the recombination coefficient A_2 can be neglected in analyzing beam scaling. We thus conclude that the axial profiles depend significantly on only two parameters, μ and initial $\bar{\kappa}$ value, $\bar{\kappa}_0$.

C. Axial Profile of the Beam and Conducting Channel for $\kappa_0 = 0$

1. General Considerations

We have solved the equations of Sec. II for cases ranging from $\mu = 0.1$ to $\mu = 100$. The $\bar{\zeta}$ dependence of the principal beam and channel features is shown in Fig. 3-5 for three typical cases with $\kappa_0 = 0$ and $\mu = 0.32, 3.2$, and 32 , corresponding approximately to 1, 10 and 100 kA beams in initially un-ionized air at standard density. In each case the beam has two distinct regions, an expanded head and a self-pinched body, with quite different structure and scale lengths. We shall proceed by showing how each of several beam properties differs qualitatively between the two regions and defining a transition point between the two regions for each property. These various transition points typically lie close together, as seen in Table 3.

At the beam head, where the gas conductivity is zero, the magnetic pinch force is canceled by electrostatic repulsion due to the beam space charge, leaving $\bar{U} = 0$. As we move back from the head of the beam, $\bar{\kappa}$ increases and the space charge begins to be neutralized by the radial outflow of plasma electrons. Nevertheless, \bar{U} is so weak throughout the head region that the beam head expands freely, constrained only by its own inertia. Within our steady state model, this rapid beam head expansion appears as a large value of $|\bar{dR}/\bar{d\zeta}|$. In the self-pinched region, on the other hand, the space charge has been completely neutralized, the beam is in pressure balance with the pinch field \bar{U} , and $|\bar{dR}/\bar{d\zeta}|$ is small. It is therefore natural to define the point where $|\bar{dR}/\bar{d\zeta}|^{-1} (d^2\bar{R}/d\bar{\zeta}^2)$ is maximal as the pinch point $\bar{\zeta}_p$.

The rapid increase in \bar{U} near $\bar{\zeta}_p$ causes a substantial induced E_z field, as is evident from Eq. (61). Beam electrons passing through this E_z "spike" lose energy rapidly, and conservation of relativistic momentum $\gamma m \dot{r}$ leads to rapid expansion of the beam ahead of the E_z spike. Thus the point $\bar{\zeta}_e$ at which E_z is maximal typically is close to $\bar{\zeta}_p$.

Since $\bar{\kappa}$ increases rapidly with $\bar{\zeta}$, the E_z spike drives a plasma return current I_p . Figs. 3-5 show that $\bar{I}_p \equiv I_p/I_b$ increases rapidly just as the space charge is being neutralized and reaches a maximum at a point $\bar{\zeta}_i$, which is close to but somewhat larger than $\bar{\zeta}_e$ because of the steadily increasing conductivity. As $\bar{\zeta}$ increases further and we enter the beam body, \bar{I}_p falls off, but if $\mu > 1$ this decrease is slow because of the rapidly increasing conductivity. In the beam body, where there is no space charge, the normalized pinch force \bar{U} reduces to $c \langle r B_\theta \rangle / I_b$ and is equal to the normalized net current $\bar{I}_n \equiv 1 - \bar{I}_p$. \bar{U} then approaches unity with a scale length $\frac{1}{8} \lambda \bar{\kappa} \bar{R}^2$ determined by resistive diffusion, as is evident from (67). By contrast, the scale length in the expanded head is determined by the conductivity generation rate $\mu \bar{R}^{-2}$ and is typically much shorter.

Even though Figs. 3c, 4c, and 5c show $\bar{U}(\bar{\zeta})$ increasing smoothly and monotonically, comparison of the $\bar{U}(\bar{\zeta})$ and $\bar{I}_n(\bar{\zeta})$ curves shows the abrupt change in the nature of the pinch force near $\bar{\zeta}_p$: in the expanded head, electrostatic forces reduce \bar{U} by partially cancelling the magnetic pinch force, but \bar{U} is purely magnetic in the

beam body. The onset of plasma return current and the rapid decrease of space charge occur in the region where $\bar{\kappa}^2 \bar{R}^2$ lies roughly between $8\lambda^{-1}$ and 8, in which the $\bar{\kappa}^2 \bar{R}^2$ terms in (67) begin to dominate. Therefore the point $\bar{\zeta}_n$ where $\lambda \bar{\kappa}^2 \bar{R}^2 / 8 = 1$ represents another transition point for the electromagnetic fields, and is typically also close to $\bar{\zeta}_p$.

Since the pinch force is in quasistatic equilibrium with the beam pressure throughout the beam body, (68) gives $\bar{U} \bar{Y} \bar{R}^2 \approx 1$ in this region. In the expanded head, where the pinch force is too weak to confine the beam, $\bar{U} \bar{Y} \bar{R}^2 \ll 1$. Figures 3b, 4b and 5b show a fairly sharp transition between these regimes. We arbitrarily define a transition point $\bar{\zeta}_{qs}$ where $\bar{U} \bar{Y} \bar{R}^2 = 0.95$. The location of $\bar{\zeta}_{qs}$ is of some significance, since it delineates the regime in which a quasistatic model of beam equilibrium is valid, for use in stability theories, for example. Although $\bar{\zeta}_{qs}$ is always fairly close to $\bar{\zeta}_p$, we find that $\bar{\zeta}_{qs} < \bar{\zeta}_p$ for $\mu \leq 1$ and $\bar{\zeta}_{qs} > \bar{\zeta}_p$ for $\mu > 1$.

The relative value of $\bar{\zeta}_p$, $\bar{\zeta}_n$, $\bar{\zeta}_i$, $\bar{\zeta}_e$ and $\bar{\zeta}_{qs}$ are given in Table 3, over a large range of μ . Several other beam properties are also summarized in Table 3, and will be discussed in the next sections.

2. Validity of the Steady State Assumption

In an actual beam, the radius R_0 at the beam head increases constantly with time, which is not strictly consistent with our steady state treatment. However, our treatment is based on the premise that, when R_0 has become much larger than the pinched radius, the value of R_0 has a negligibly small effect on all beam properties in the region of interest, where $R \ll R_0$. This premise was supported by the observation in Sec. IIF that as $\tilde{\beta} \rightarrow \beta$, large changes in R_0 correspond to very small changes in $\tilde{\beta}$. It is also necessary that $R(\zeta)$, $\gamma(\zeta)$ and $\kappa(\zeta)$ converge to steady state values when $R_0 \geq R_p$, where R_p is the radius at the pinch point. This requirement is also found to be well satisfied in the numerical solutions. As an example, Fig. 6 shows $\bar{R}(\zeta/R_\infty)$ for a typical case, obtained by the method described in Sec. IIF, using three slightly differing value of $\tilde{\beta}$. Even though the $\tilde{\beta}$ variation results in very different values of R_0 , $\bar{R}(\zeta/R_\infty)$ profiles are nearly identical when $R_0 \geq 10R_p$. We may therefore describe the time during which the beam propagates from its source until R_0 reaches the order of $10R_p$ as a period of transient beam head expansion. Time-dependent treatments have indicated that this initial transient expansion occurs considerably faster than the steady state erosion that follows.¹⁻⁵

3. Scaling of Beam Profile and Fractional Return Current

with μ

In the beam body, the degree of beam pinching, i.e. the value of the dimensionless radius \bar{R} , depends on the fractional plasma return current \bar{I}_p . Although it is always true that $\bar{R} \rightarrow 1$ and $\bar{I}_p \rightarrow 0$ as $\bar{\zeta}$ becomes very large, the values of \bar{R} at $\bar{\zeta}_p$ and of \bar{I}_p at its maximum point $\bar{\zeta}_1$ are indicative of conditions over a substantial length of the beam body: A beam is tightly pinched throughout the body if $\bar{R}(\bar{\zeta}_p) \approx 1$, whereas a beam with $\bar{R}(\bar{\zeta}_p) \gg 1$ may be described as weakly pinched. The numerical results tabulated in Table 3 indicate that

$$\bar{R}(\bar{\zeta}_p) \approx 1 + \mu \quad (72)$$

for $0.1 \leq \mu \leq 100$. A beam is therefore seen to be well-pinchd if $\mu < 1$ and weakly pinched if $\mu > 1$, in agreement with many experimental observations that beams tend to be weakly pinched when the conductivity rises too rapidly.

Figures 3-5 and Table 3 further suggest that the axial profiles $\bar{R}(\bar{\zeta})$, $\bar{U}(\bar{\zeta})$ and $\bar{\kappa}(\bar{\zeta})$ can be characterized in the region $\bar{\zeta} \leq \bar{\zeta}_p$ by very approximate self-similar expressions with μ as a scaling parameter. To obtain such scalings, we assume forms

$$\bar{R} = \mu^{n_1} f_1(\mu^{m_1} \bar{\zeta}) \quad , \quad (73a)$$

$$\bar{U} = \mu^{n_2} f_2(\mu^{m_2} \bar{\zeta}) \quad , \quad (73b)$$

$$\bar{\kappa} = \mu^{n_3} f_3(\mu^{m_3} \bar{\zeta}) \quad , \quad (73c)$$

and we neglect both the recombination term $A_2 \bar{\rho}^2 \bar{\kappa}^2$ in (70) and the $\bar{\kappa}^2 \bar{R}^2$ terms in (67). We choose the coefficient n_1 to be consistent with (72) and require that $n_2 = -n_1$, so that the beam can reach quasistatic equilibrium at $\bar{\zeta} \approx \bar{\zeta}_p$. To satisfy the requirements of self-similarity, we must also choose the radius \bar{R}_0 at the beam head to be some fixed multiple of \bar{R}_p . The only possible scaling of (67) - (70) that is consistent with these requirements is

$$\bar{R} = f_1(\mu^{1/2} \bar{\zeta}), \quad (74a)$$

$$\bar{U} = f_2(\mu^{1/2} \bar{\zeta}), \quad (74b)$$

$$\bar{\kappa} = \mu^{1/2} f_3(\mu^{1/2} \bar{\zeta}), \quad (74c)$$

for $\mu \ll 1$, and

$$\bar{R} = \mu F_1(\bar{\zeta}), \quad (75a)$$

$$\bar{U} = \mu^{-1} F_2(\bar{\zeta}), \quad (75b)$$

$$\bar{\kappa} = \mu^{-1} F_3(\bar{\zeta}), \quad (75c)$$

for $\mu \gg 1$. Neither scaling is exact, but both are useful, and the numerical solutions illustrated in Figs. 3-5 and Table 3 verify their approximate validity.

These scaling laws yield several types of information about the beam evolution. (i) They indicate how the axial profile of the beam depends on the parameter μ : the "trumpet" shape of the expanded head becomes more extreme as μ increases. (ii) We have argued that the beam passes through a transient period of very rapid expansion, during

which \bar{R}_0 increases to approximately $10\bar{R}(\zeta_p)$, before the steady state is established. The extent in $\bar{\zeta}$ of the expanded region is thus equal to $\bar{\zeta}_p$ when $\bar{R}_0 \sim 10\bar{R}(\bar{\zeta}_p)$. The scaling relations (74) and (75) indicate that this region scales as $\mu^{1/2}$ for $\mu < 1$ and reaches a constant value for $\mu > 1$. However, (75) also indicates that the body of the beam expands a great deal if $\mu \gg 1$. (iii) An electron which was originally located in the pinched body of the beam, $\zeta > \zeta_p$, but which later finds itself in the expanding nose as the pinch point moves back into the beam, will in general escape radially at a velocity less than its original transverse thermal velocity, because the expanding beam does work against the magnetic field. According to (74) and (75), the escape velocity scales as

$$\frac{dR}{dt} = (1-\beta)c \left| \frac{dR}{d\zeta} \right| \propto \mu^{1/2} \lambda_{\infty} I_D / \gamma_{\infty}, \quad \mu < 1 \quad (76a)$$

$$\propto \mu \lambda_{\infty} I_D / \gamma_{\infty}, \quad \mu > 1. \quad (76b)$$

D. Axial Profiles and Scaling for $\kappa_0 \neq 0$

When the background gas is sufficiently preionized to neutralize the beam space charge, the beam still has a freely expanding head and approaches steady-state erosion. However, the fields are quite different from a case with $\kappa_0 = 0$, and we find significantly different scaling laws. Since $\lambda \bar{\kappa}_0^2 \bar{R}_{po}^2 / 8 \leq 1$ for $\bar{\zeta} < \bar{\zeta}_p$ when $\bar{\kappa}_0 = 0$, a condition that $\bar{\kappa}_0$ dominate beam-generated conductivity for all $\bar{\zeta} < \bar{\zeta}_p$ is that

$$\lambda \bar{\kappa}_0^2 \bar{R}_{po}^2 / 8 > 1, \quad (77a)$$

where \bar{R}_{po} is $\bar{R}(\bar{\zeta}_p)$ for the beam when $\kappa_0 = 0$. Using (72) for \bar{R}_{po} , this condition becomes

$$\lambda \bar{\kappa}_0^2 / 8 > 1, \quad \text{if } \mu < 1, \quad (77b)$$

$$\lambda \bar{\kappa}_0^2 \mu^2 / 8 > 1, \quad \text{if } \mu > 1. \quad (77c)$$

When (77) is satisfied, the beam is space-charge neutralized essentially everywhere, so that $\bar{U} = \bar{I}_n$. Nevertheless, $\bar{U} = 0$ at the beam head because the plasma return current generated there completely cancels the beam current. The absence of a pinch force at the beam head leads to free expansion of the head and subsequently to steady state erosion, just as in the case with $\kappa_0 = 0$. Although the erosion rate is independent of both κ_0 and μ , as we have seen in Sec. IIIB, the $\bar{R}(\bar{\zeta})$ profile is modified by κ_0 . As long as $\bar{\kappa} \approx \bar{\kappa}_0$, the scale length for the rise of \bar{I}_n is $\frac{1}{8} \lambda \bar{\kappa}_0^2 \bar{R}^2$. The only possible self-similar

scaling for $\bar{R}(\bar{\zeta})$, $\bar{I}_n(\bar{\zeta})$, and $\bar{U}(\bar{\zeta})$ is then

$$\bar{R}(\bar{\zeta}) = f_1(\bar{\zeta}/\kappa_0) \quad (78a)$$

$$\bar{I}_n(\bar{\zeta}) = \bar{U}(\bar{\zeta}) = f_2(\bar{\zeta}/\kappa_0), \quad (78b)$$

where f_1 and f_2 are independent of μ . The beam pinches down more slowly than in un-ionized gas, and so for any value of $\bar{\zeta}$, $\bar{R}(\bar{\zeta})$ is larger than it would be for $\kappa_0 = 0$. These features are illustrated by the plots of $\bar{R}(\bar{\zeta})$ and $\bar{I}_n(\bar{\zeta})$ in Fig. 7 for cases with $\mu = 0.2$ and in Fig. 8 for $\mu = 5$.

For cases in which $\bar{\kappa}_0$ is nonzero but not large enough to satisfy (77), the pre-existing conductivity can modify the beam properties in a limited region of the expanded head, but will have little or no influence on the beam body. For sufficiently large \bar{R}_0 , even a small $\bar{\kappa}_0$ can result in a value of $\bar{\kappa}\bar{R}$ near the beam head large enough to neutralize the space charge there. However, $\lambda\bar{\kappa}^2\bar{R}^2/8$ decreases at large $\bar{\zeta}$ values as \bar{R} decreases, and space charge forces can reappear at some $\bar{\zeta} < \bar{\zeta}_p$. This results in the somewhat complicated $\bar{I}_n(\bar{\zeta})$ curves for $\bar{\kappa}_0 = 0.07$ in Figs. 7b and 8b. When $\mu < 1$, Eq. (74) indicates that the beam tends to pinch down faster when conductivity is increased. Thus a small non-zero value of $\bar{\kappa}_0$ increases $|d\bar{R}/d\bar{\zeta}|$ near the beam head, just as a small increase in μ would. However, in the part of the beam where $\bar{\kappa} > \bar{\kappa}_0$ the $\bar{R}(\bar{\zeta})$ curves have the form they would have for $\bar{\kappa}_0 = 0$ but are shifted toward the head, as Fig. 7a shows. In particular, $\bar{R}(\bar{\zeta})$ at and behind the pinch point is unchanged by $\bar{\kappa}_0$.

When $\mu > 1$, $d\bar{R}/d\bar{\zeta}$ is insensitive to small changes in conductivity, and if (77) is not satisfied the entire $\bar{R}(\bar{\zeta})$ curve is essentially independent of $\bar{\kappa}_0$, as seen in Fig. 8a.

IV. Summary

The pinch frame formalism presented here is an efficient and conceptually simple method for calculating the beam head erosion rates and axial profiles of relativistic electron beams. The principal shortcomings of the method are the non-selfconsistent treatment of emittance and energy changes due to collisions and radiation, and an inability to model early transient expansion of the beam head. Nonetheless the formalism gives usable information about beam structure and an unambiguous erosion rate value without requiring time-dependent calculations.

We have examined relativistic electron beams with a wide range of parameters and can make several generalizations:

1) If energy loss and expansion from collisions and radiation are neglected, erosion continues at a steady rate after initial transient expansion of the head. For a constant-current pulse, this rate is $\frac{\lambda_{\infty}}{\gamma(\zeta)} \frac{|I_n(\zeta)|}{17kA} c$, where ζ is any point well behind the pinch point. The radial dependences of beam density and conductivity and the maximum radius of the conductivity channel R_c affect erosion rates only weakly by altering the beam inductance λ_{∞} .

2) When the background gas is initially un-ionized and the current is high enough that $\kappa_{\infty} R_{\infty} \gg 1$, then the beam axial profile near the beam head is controlled principally by the dimensionless parameter $\mu = 4\pi R^2 c^{-1} d\langle\sigma\rangle/d\zeta$ that controls conductivity generation. For air with ionization caused by beam-molecule collisions,

$\mu \approx 3 \times 10^{-4} |I_b| (2\text{eV}/T_e)^{1/2}$. When $\mu \ll 1$, the peak return current is small compared with I_b , and the beam pinches to $R \approx R_\infty$. In contrast, the return current is comparable with I_b when $\mu \gg 1$ and the radius at the pinch point is approximately μR_∞ .

3) When the initial gas conductivity $\bar{\kappa}_0$ is large compared with beam-generated conductivity throughout the beam head, the beam space charge and current are neutralized essentially at ζ_0 . The beam pinches with a scale length $\lambda \bar{\kappa}_0 \bar{R}^2/8$. Although there is no distinct pinch point, beam head erosion proceeds at the same rate as for $\bar{\kappa}_0 = 0$.

APPENDIX

The erosion rate calculations in Section IIIA are limited to conditions for which $(1-\beta) \leq 0.2$ by the $\beta \approx 1$ approximation made in deriving the field equations (35)-(39). We can estimate the rate for lower $|I_b|/\gamma_\infty$ values by using the field equations (23)-(25), which do not assume $\beta \approx 1$. Integrating (24) over the entire beam gives

$$r \frac{\partial}{\partial r} \int_{\zeta}^{\infty} d\zeta E_z(r, \zeta) = \frac{2}{c} [\beta I_\infty(r) + (1-\beta) I_0(r)], \quad (A1)$$

where we have used the boundary values $E_z(r, 0) = E_z(r, \infty) = 0$ and $u(r, \infty) = rB_\theta(r, \infty)$ and have eliminated rB_θ with (25). If we assume that the left side of (A1) has the same radial dependence as $I(r)$, then the equation can be radially averaged at $\zeta = \infty$ to give

$$-\frac{1}{(\lambda_\infty)^{1/2}} \int_{\zeta}^{\infty} d\zeta \frac{\langle E_z \rangle}{(\lambda_\infty)^{1/2}} = \frac{2}{c} [\beta \langle I_\infty \rangle + (1-\beta) \langle I_0 \rangle] \quad (A2)$$

where $\langle I_\infty(r) \rangle = \frac{1}{2} I_b$ for any of the radial density profiles treated here. Since $I_0(r)$ is the current within radius r at the expanded beam head, the average of I_0 over the number density at $\zeta = \infty$ is smaller than $I_b/2$ by approximately the ratio $R_\infty^2/R_0^2 \ll 1$, and the $\langle I_0 \rangle$ term in (A2) is negligible. If we again ignore the change of inductance along the length of the beam, then we may set $\lambda(\zeta) \approx \lambda_\infty$ in (A2) and obtain

$$\int_{\zeta_0}^{\infty} d\zeta' \langle E_z' \rangle \approx \frac{\beta \lambda_{\infty} |I_b|}{c}. \quad (A3)$$

Substituting this approximation into (3.1) gives

$$\Delta\gamma \approx \frac{\beta}{1-\beta} \frac{e\lambda_{\infty} |I_b|}{mc^3}, \quad (A4)$$

which differs from the $\beta = 1$ result (3.4) only by the β factor on the right side. The corresponding expression for the limiting erosion rate is

$$1-\beta \approx \left(1 + \frac{mc^3}{e} \frac{\gamma_{\infty}^{-1}}{\lambda_{\infty} I_b} \right)^{-1} \quad (A5)$$

This expression agrees with (64) for $1-\beta \ll 1$ and should be valid over a wider range of $|I_b|$ and γ_{∞} . The principal restriction on (A5) is that γ_{∞} must be large enough that the ultrarelativistic approximation $v_z \approx c$ is satisfied over most of the beam.

Acknowledgments

We are grateful to Adam T. Drobot for useful discussions of numerical methods.

This work was sponsored by the Defense Advanced Research Projects Agency (DOD) under ARPA Order No. 3718, Amendment No. 12.

References

1. R. Biegalski (private communication).
2. E. P. Lee (private communication).
3. K. A. Brueckner (private communication).
4. R. F. Hubbard, D. S. Spicer, J. C. Guillory, and D. A. Tidman
"Classical Model of High-Current Beam Propagation", JAYCOR Report
350-79-012 (1979).
5. R. R. Johnston, R. L. Feinstein, D. E. Maxwell, E. R. Parkinson,
and E. E. Simpson (private communication).
6. M. I. Haftel, M. Lampe, and J. B. Aviles, Phys. Fluids 22, 2216
(1979).
7. E. P. Lee and R. K. Cooper, Particle Accelerators 7, 83 (1976).
8. W. H. Bennett, Phys. Rev. 45, 890 (1934).
9. B. Rossi, High Energy Particles (Prentice-Hall, New York, 1952),
pp. 27 and 55.
10. B. Rossi, Op.Cit., p.67.

Table 1. Typical $v_m/\bar{\rho}$ values and direct-ionization coefficients for air, He, Ne, and Ar. A background electron temperature of 2eV is assumed.

<u>Gas</u>	<u>Beam Energy (MeV)</u>	<u>$v_m/\bar{\rho}$ (sec⁻¹)</u>	<u>\hat{A}_1 (cm⁻¹sec⁻¹)</u>	<u>A_1 (cm²kA⁻¹)</u>
Air	50	2.0×10^{12}	6.0×10^{20}	0.34
Air	5	2.0×10^{12}	4.3×10^{20}	0.24
He	5	1.3×10^{12}	2.9×10^{20}	0.25
Ne	5	3.2×10^{11}	1.3×10^{20}	0.45
Ar	5	2.0×10^{11}	2.4×10^{19}	0.14

Table 2. Comparison of calculated erosion rates with analytic estimates for $R_\infty = 0.2$ cm and $R_c = 20$ cm. The parameters I_b and R_∞ were chosen to fall in the range spanned by the new generation of linear induction accelerators at Lawrence Livermore Laboratory, the Experimental Test Accelerator ($\gamma \sim 10$) and Advanced Test Accelerator ($\gamma \sim 100$) and to cover a broad energy range.

Density Profile	I_b (kA)	γ_∞	Calculated $1-\beta$	Analytic $1-\beta$
Gaussian	10	1000	4.7×10^{-3}	5.3×10^{-3}
	10	500	9.4×10^{-3}	1.1×10^{-2}
	10	200	2.4×10^{-2}	2.7×10^{-2}
	10	100	4.8×10^{-2}	5.5×10^{-3}
	10	50	9.6×10^{-2}	1.1×10^{-1}
	10	20	2.6×10^{-1}	2.8×10^{-1}
	20	100	9.6×10^{-2}	1.1×10^{-1}
	5	100	2.4×10^{-2}	2.7×10^{-2}
Bennett	10	100	4.3×10^{-2}	5.5×10^{-2}
Square	10	100	5.4×10^{-2}	5.5×10^{-2}

Table 3. Profile data for beams in initially un-ionized gas. In each case $\beta = 0.05$. For $\mu = 0.1$ to 32, $\bar{R}_0 \approx 10\bar{R}(\bar{\zeta}_p)$ is chosen to facilitate comparison with the self-similar scaling laws (74) and (75). For $\mu = 100$, $\bar{R}_0 \ll 10\bar{R}(\bar{\zeta}_p)$ is used for reasons of numerical efficiency, and as a result all $\bar{\zeta}$ points are shifted toward zero.

μ	\bar{R}_0	$\bar{R}(\bar{\zeta}_p)$	$\bar{R}(5\bar{\zeta}_p)$	$\bar{I}_p(\bar{\zeta}_i)$	$\bar{\zeta}_p$	$\bar{\zeta}_n$	$\bar{\zeta}_e$	$\bar{\zeta}_i$	$\bar{\zeta}_{qs}$
0.1	11.4	1.1	1.0	0.09	56	50	45	46	29
0.32	13.5	1.3	1.0	0.20	36	27	29	32	20
1.0	21.5	2.1	1.2	0.41	27	19	24	27	21
3.2	50.6	4.7	1.9	0.64	24	18	23	28	25
10	121.9	11.9	4.1	0.82	21	16	22	30	30
32	293.2	29.1	10.4	0.91	21	20	22	31	35
100	324.8	94.1	53.5	0.98	4	6	7	18	46

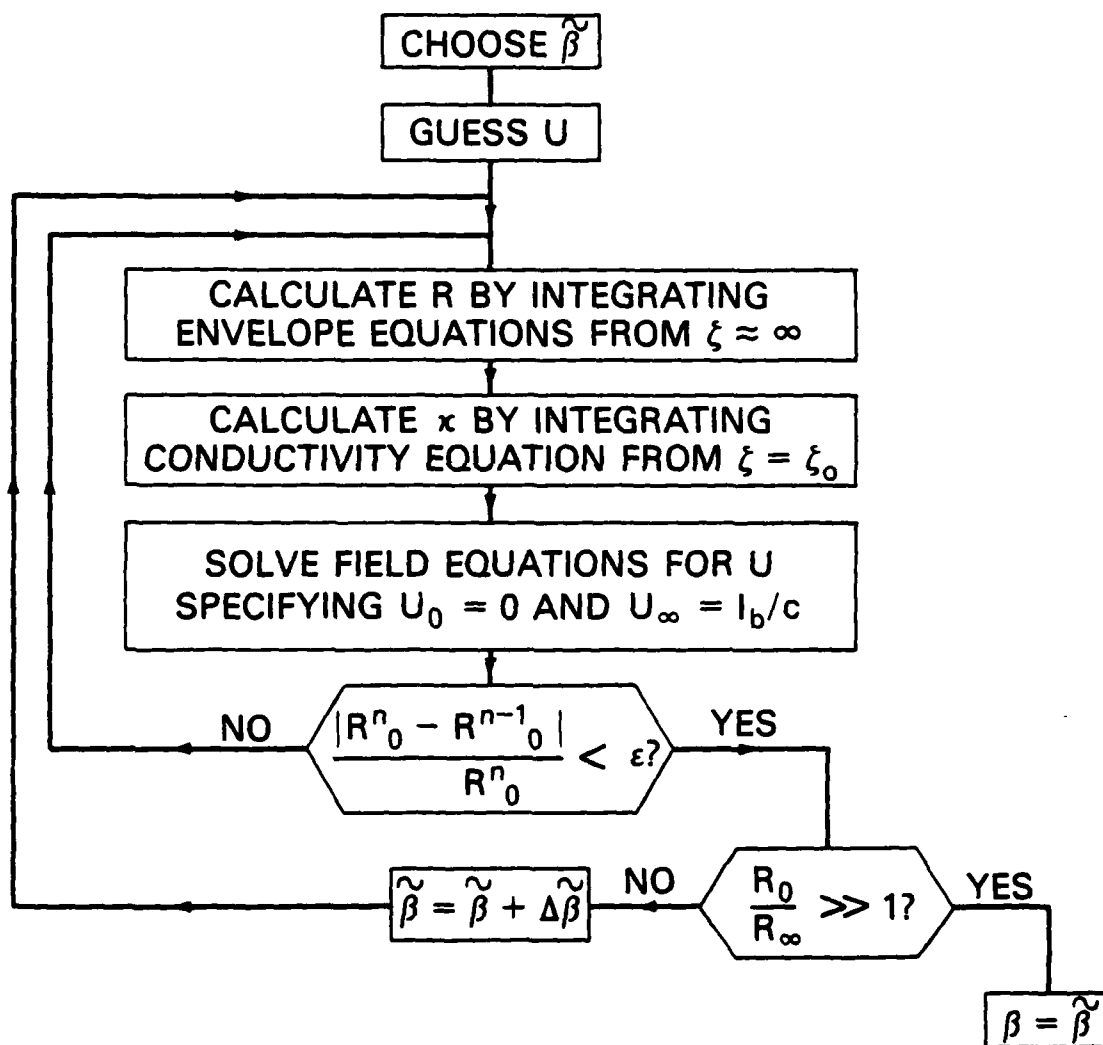


Fig. 1 - Method of solution of the steady-state beam equations

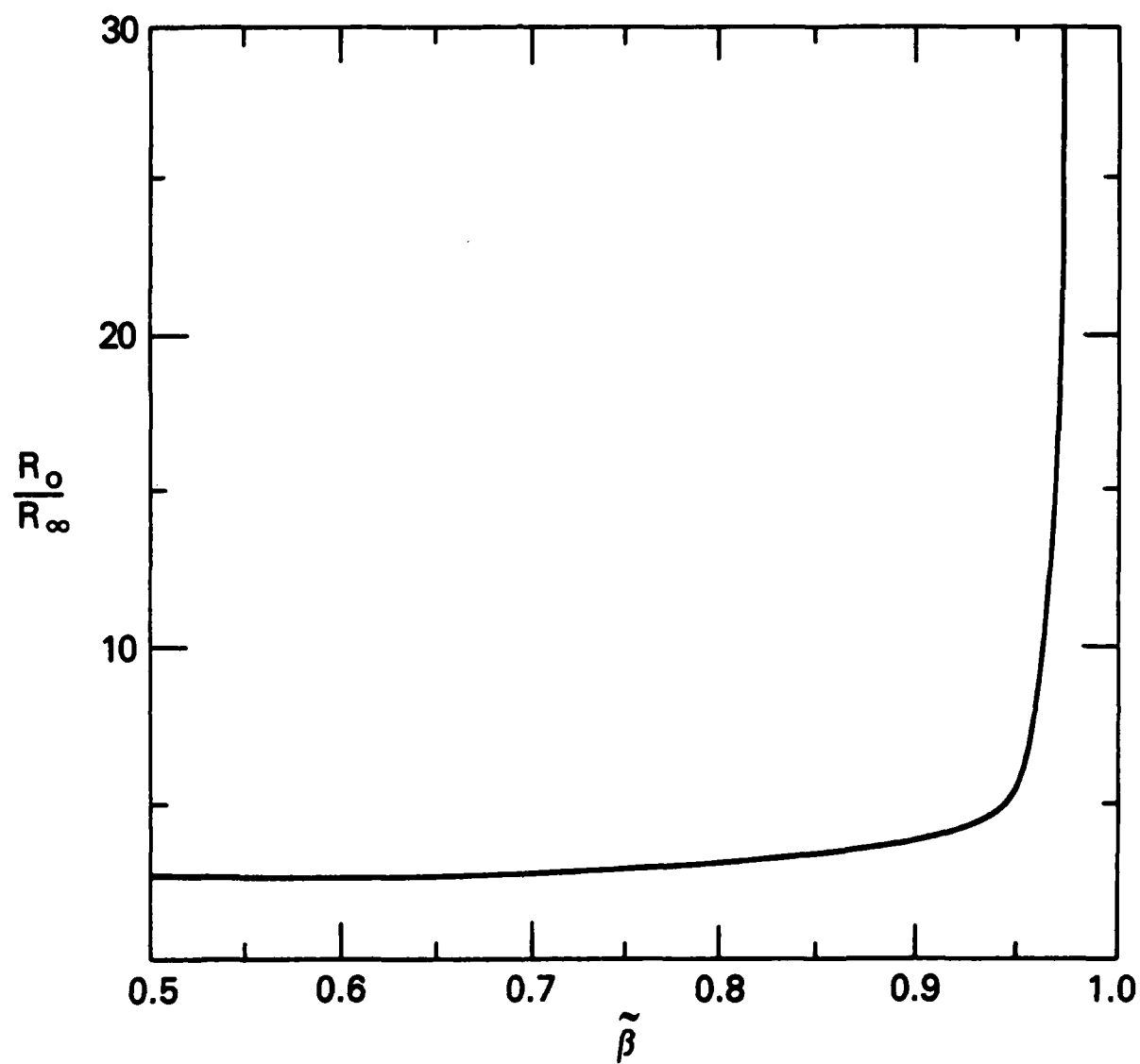
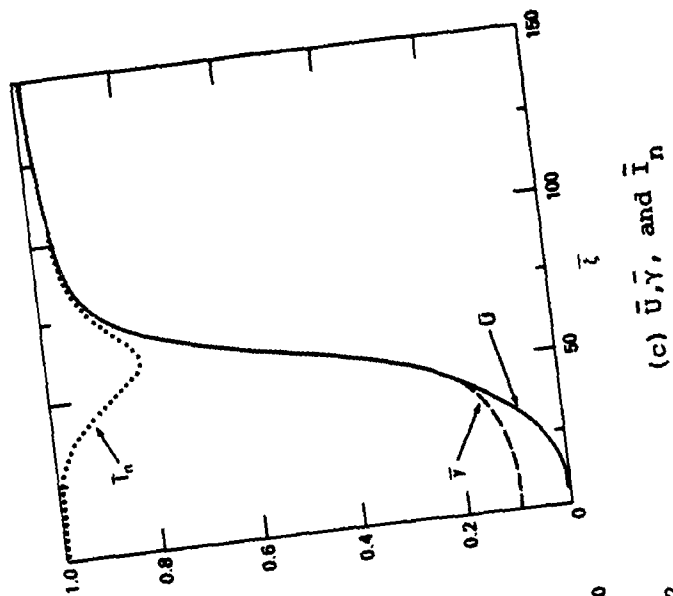
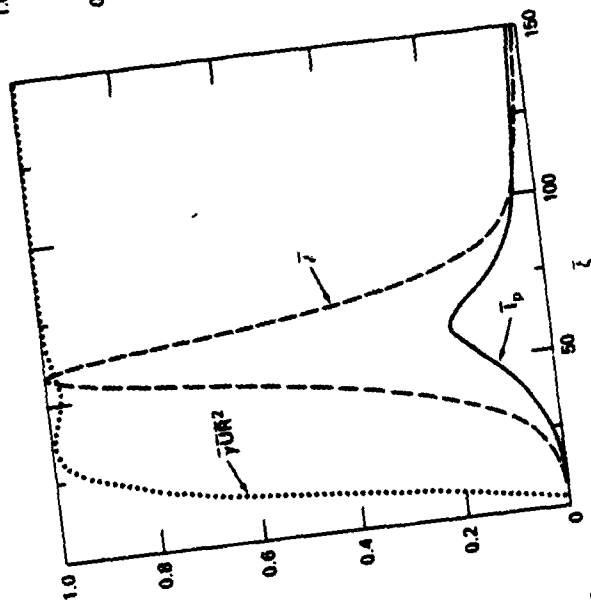


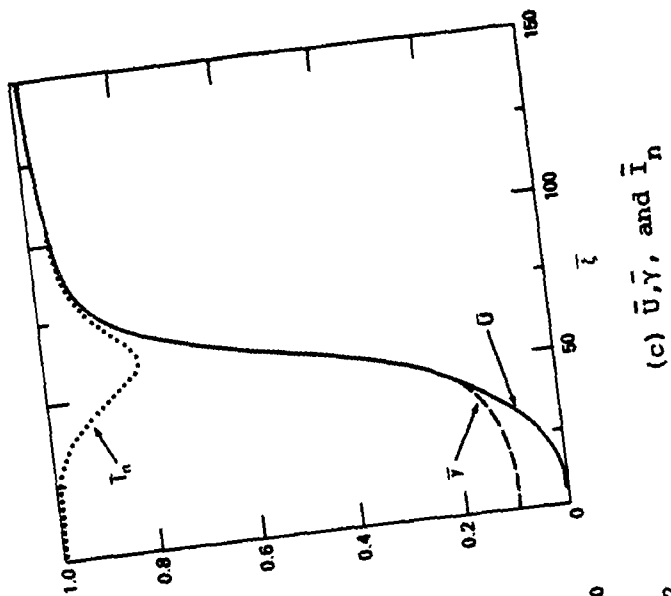
Fig. 2 - Variation of calculated beam head radius R_0 with $\tilde{\beta}$



(a) \bar{R} and $\bar{\kappa R}$



(b) $\bar{E} \equiv E_z/\max E_z, \bar{I}_p, \text{ and } \gamma UR^2$



(c) $\bar{U}, \bar{\gamma}, \text{ and } \bar{I}_n$

Fig. 3 - Beam axial profile for $\mu = 0.32$ and $\bar{\kappa}_0 = 0$:

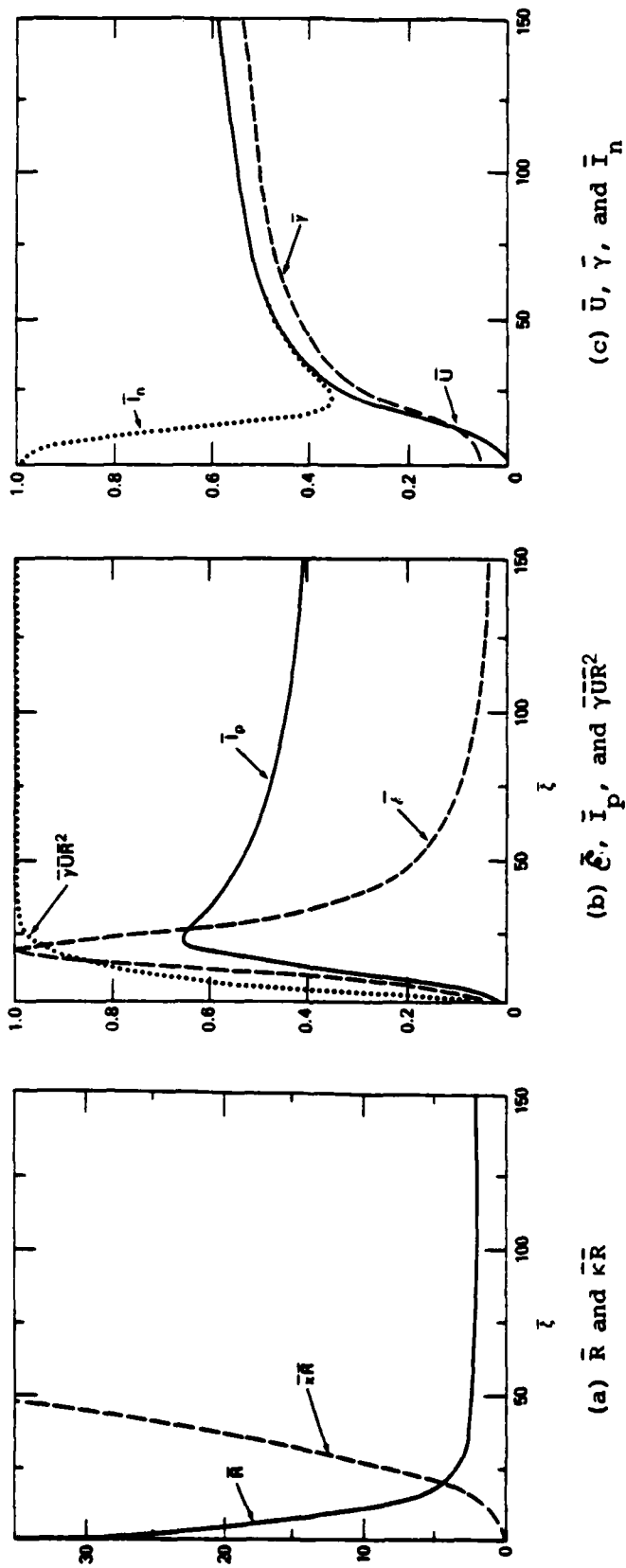
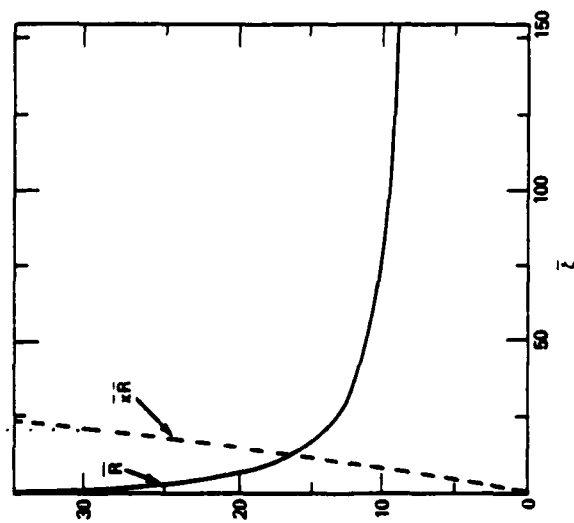
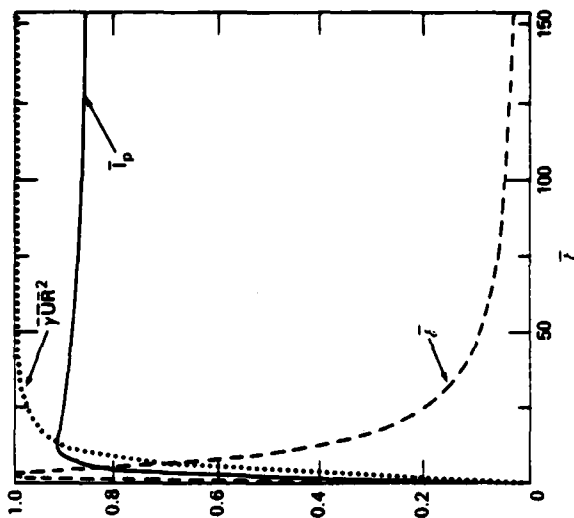


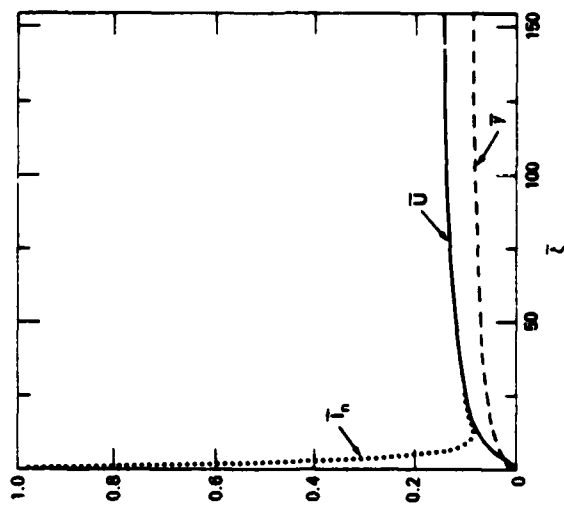
Fig. 4 - Beam axial profile for $\mu = 3.2$ and $\bar{k}_0 = 0$



(a) \bar{R} and $\bar{\kappa R}$



(b) $\tilde{\gamma}$, \tilde{I}_p , and $\tilde{\gamma UR^2}$



(c) \bar{U} , $\tilde{\gamma}$, and \tilde{I}_n

Fig. 5 - Beam axial profile for $\mu = 32$ and $\bar{\kappa}_0 = 0$

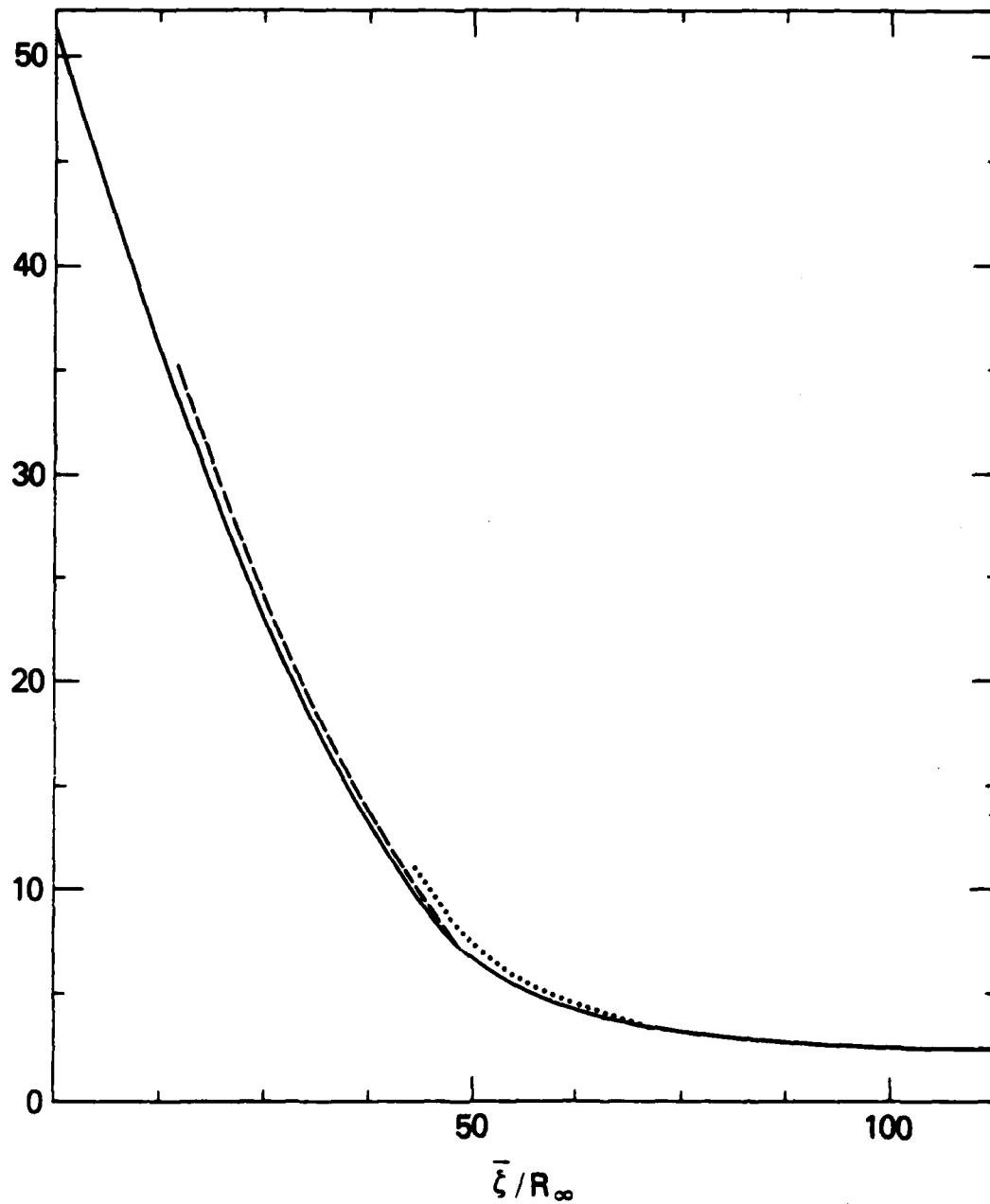
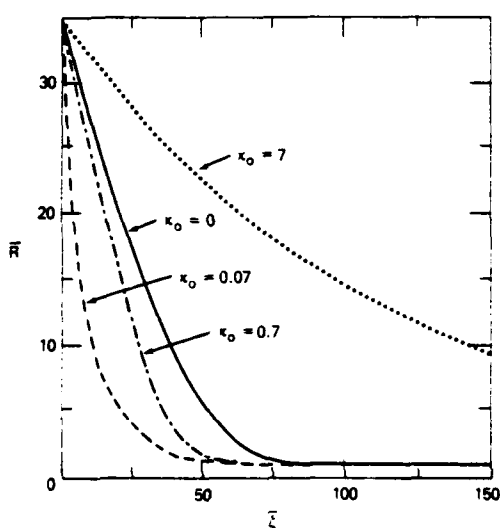
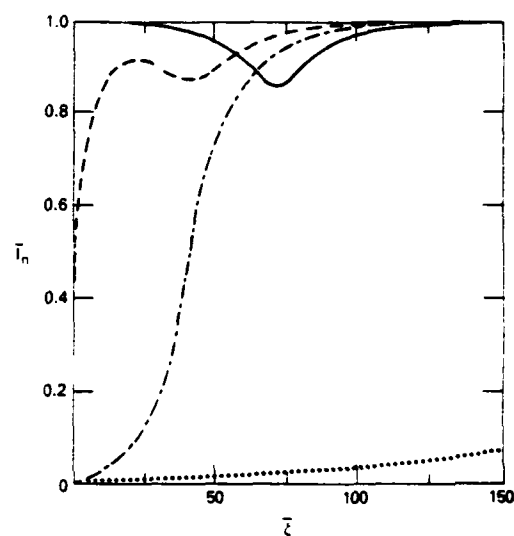


Fig. 6 - $\bar{R}(\bar{\zeta})$ for a beam with $\mu = 3.2$ for three $\bar{\beta}$ values near β .

Calculated axial profiles near the pinch point are seen to be insensitive to changes in \bar{R}_0 when $\bar{R}_0 \gg \bar{R}_p$.

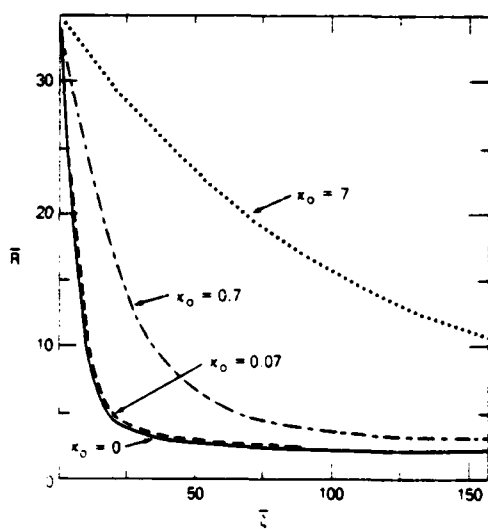


(a) \bar{R}

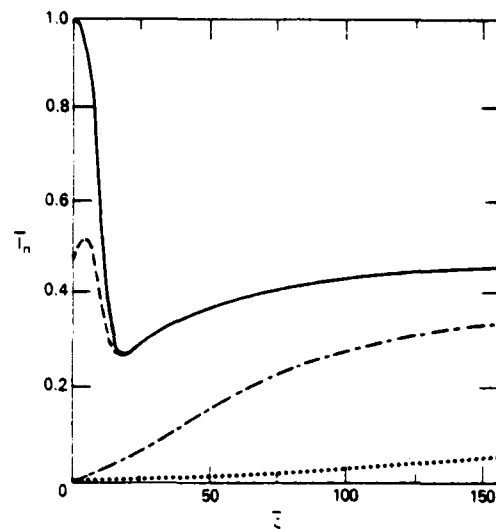


(b) \bar{I}_n

Fig. 7 - Variation of beam axial profile with κ_0 when $\mu = 0.2$



(a) \bar{R}



(b) \bar{I}_n

Fig. 8 - Variation of beam axial profile with κ_0 when $\mu = 5$

DISTRIBUTION LIST

1. Commander
Naval Sea Systems Command
Department of the Navy
Washington, D.C. 20363
Attn: NAVSEA 03H (Dr. C. F. Sharn)
2. Central Intelligence Agency
P. O. Box 1925
Washington, D.C. 20013
Attn: Dr. C. Miller/OSI
3. Air Force Weapons Laboratory
Kirtland Air Force Base
Albuquerque, New Mexico 87117
Attn: Lt. Col. J. H. Havey
4. U. S. Army Ballistics Research Laboratory
Aberdeen Proving Ground, Maryland 21005
Attn: Dr. D. Eccleshall (DRXBR-BM)
5. Ballistic Missile Defense Advanced Technology Center
P. O. Box 1500
Huntsville, Alabama 35807
Attn: Dr. L. Havard (BMDSATC-1)
6. B-K Dynamics, Inc.
15825 Shady Grove Road
Rockville, Maryland 20850
Attn: Mr. I. Kuhn
7. Intelcom Rad Tech
P. O. Box 81087
San Diego, California 92138
Attn: Mr. W. Selph
8. Lawrence Livermore Laboratory
University of California
Livermore, California 94550
Attn: Dr. R. J. Briggs
Dr. T. Fessenden
Dr. E. P. Lee
9. Mission Research Corporation
735 State Street
Santa Barbara, California 93102
Attn: Dr. C. Longmire
Dr. N. Carron

10. National Bureau of Standards
Gaithersburg, Maryland 20760
Attn: Dr. Mark Wilson
11. Science Applications, Inc.
1200 Prospect Street
La Jolla, California 92037
Attn: Dr. M. P. Fricke
Dr. W. A. Woolson
12. Science Applications, Inc.
Security Office
5 Palo Alto Square, Suite 200
Palo Alto, California 94304
Attn: Dr. R. R. Johnston
Dr. Leon Feinstein
13. Science Applications, Inc.
1651 Old Meadow Road
McLean, Virginia 22101
Attn: Mr. W. Chadsey
14. Science Applications, Inc.
8201 Capwell Drive
Oakland, California 94621
Attn: Dr. J. E. Reaugh
15. Naval Surface Weapons Center
White Oak Laboratory
Silver Spring, Maryland 20910
Attn: Mr. R. J. Biegalski
Dr. R. Cawley
Dr. J. W. Forbes
Dr. D. L. Love
Dr. C. M. Huddleston
Dr. G. E. Hudson
Mr. W. M. Hinckley
Mr. G. J. Peters
Mr. N. E. Scofield
Dr. E. C. Whitman
Dr. M. H. Cha
Dr. H. S. Uhm
Dr. R. Fiorito
16. C. S. Draper Laboratories
Cambridge, Massachusetts 02139
Attn: Dr. E. Olsson
Dr. L. Matson
17. M.I.T. Lincoln Laboratories
P. O. Box 73
Lexington, Massachusetts 02173
Attn: Dr. J. Salah

18. Physical Dynamics, Inc.
P. O. Box 1883
La Jolla, California 92038
Attn: Dr. K. Brueckner
 19. Office of Naval Research
Department of the Navy
Arlington, Virginia 22217
Attn: Dr. W. J. Condell (Code 421)
 20. Avco Everett Research Laboratory
2385 Revere Beach Pkwy.
Everett, Massachusetts 02149
Attn: Dr. R. Patrick
Dr. Dennis Reilly
 21. Defense Technical Information Center
Cameron Station
5010 Duke Street
Alexandria, VA 22314 (12 copies)
 22. Naval Research Laboratory
Washington, D.C. 20375
- M. Lampe - Code 4792 (50 copies)
M. Friedman - Code 4700.1
J. R. Greig - Code 4763
I. M. Vitkovitsky - Code 4770
J. B. Aviles - Code 4665
M. Haftel - Code 4665
T. Coffey - Code 4000
Superintendent, Plasma Physics Div. - Code 4700 (25 copies)
Branch Head, Plasma Theory Branch - Code 4790
Library - Code 2628
A. Ali - Code 4700.1
D. Book - Code 4040
J. Boris - Code 4040
I. Haber - Code 4790
S. Kainer - Code 4790
A. Robson - Code 4760
P. Sprangle - Code 4790
D. Colombant - Code 4790
M. Picone - Code 4040
D. Spicer - Code 4169
M. Raleigh - Code 4760
R. Pechacek - Code 4763

23. Defense Advanced Research Projects Agency
1400 Wilson Blvd.
Arlington, VA 22209
Attn: Dr. J. Mangano
Dr. J. Bayless
24. JAYCOR
205 S. Whiting St.
Alexandria, VA 22304
Attn: Drs. D. Tidman
R. Hubbard
J. Guillory
25. JAYCOR
Naval Research Laboratory
Washington, D.C. 20375
Attn: Dr. R. Fernsler - Code 4770
Dr. G. Joyce - Code 4790
Dr. S. Goldstein - 4770
26. SAI
Naval Research Laboratory
Washington, D.C. 20375
Attn: A. Drobot - Code 4790
W. Sharp - Code 4790
27. Physics International, Inc.
2700 Merced Street
San Leandro, CA.
Attn: Drs. S. Putnam
E. Goldman
28. Mission Research Corp.
1400 San Mateo, S.E.
Albuquerque, NM 87108
Attn: Dr. Brendan Godfrey
29. Princeton University
Plasma Physics Laboratory
Princeton, NJ 08540
Attn: Dr. Francis Perkins, Jr.
30. McDonnell Douglas Research Laboratories
Dept. 223, Bldg. 33, Level 45
Box 516
St. Louis, MO 63166
Attn: Dr. Michael Greenspan

31. Cornell University
Ithaca, NY 14853
Attn: Prof. David Hammer
32. Sandia Laboratories
Albuquerque, NM 87185
Attn: Dr. Bruce Miller
Dr. Barbara Epstein
33. University of California
Physics Department
Irvine, CA 92717
Attn: Dr. Gregory Benford
34. Defense Technical Information Center
Cameron Station
5010 Duke Street
Alexandria, VA 22314 (12 copies)
35. Beers Associates Inc.
Attn: Dr. Douglas Strickland
P. O. Box 2549
Reston, Va, 22090